Gag-ZiL and ΔNC-Gag). We found ΔNC-Gag-GFP (coexpressed with ΔNC-Gag in a 1:3 ratio) in WT cells was more widely distributed and less punctate at the PM than when Gag-GFP was expressed (Fig. 2 *A* and *C*). Moreover, in ΔNC-Gag-GFP–expressing cells, very little viral RNA (assessed by FISH of ΔNC viral RNA) colocalized with ΔNC-Gag at the PM (Fig. 2 *B* and *C*). In addition, spt-PALM analysis showed ΔNC-Gag to be much more mobile than Gag in WT cells, with mobile ΔNC-Gag molecules having a mean diffusion coefficient of 0.56 ± 0.03 $\mu m^2/s$ compared with Gag molecules having a diffusion coefficient of ~0.10 $\mu m^2/s$ (Fig. 2*D*). PALM cluster analysis further revealed that less than 1% of ΔNC-Gag molecules form clusters. Thus, when the NC domain of Gag is deleted, viral RNA recruitment to the PM is inhibited, Gag increases its mobility at the PM, and Gag coalescence into tight clusters is impeded.

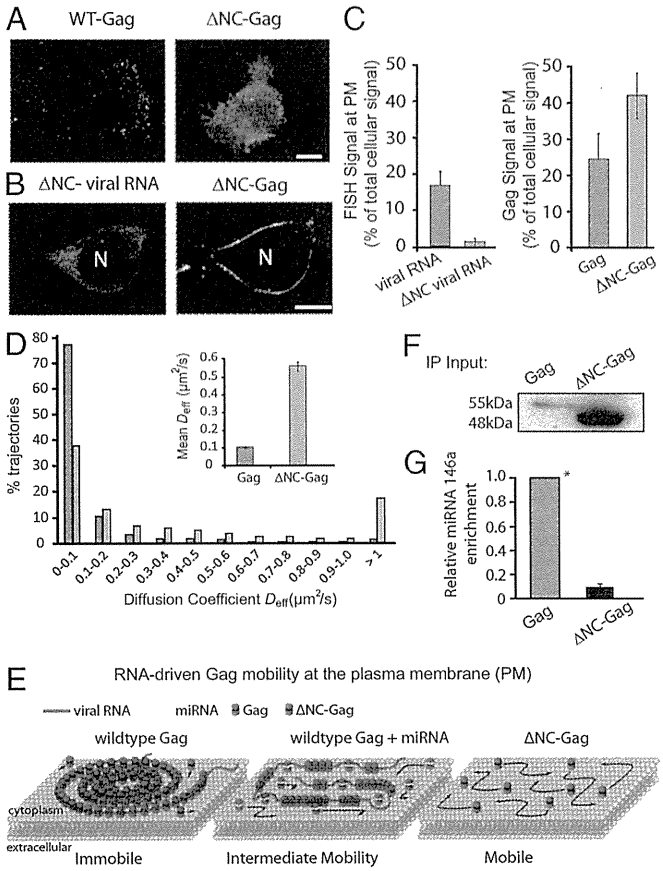

Fig. 2. miRNAs interact with the nucleocapsid (NC) domain of Gag to disrupt Gag assembly. (*A*) Representative TIRF images of Gag or ΔNC-Gag at the PM in WT cells. (*B*) WT cells were transfected with pNL43ΔPolΔNC-Gag-GFP, which has the NC domain of Gag deleted. Confocal images of unspliced HIV-1 viral RNA detected by FISH (*Left*) and ΔNC-Gag-GFP detected by fluorescence (*Right*). Note that viral RNA is distributed cytoplasmically, whereas ΔNC-Gag is enriched at the PM in these cells. (*C*) Quantification of HIV-1 viral RNA (assessed by FISH) and Gag (assessed by GFP signal) at the PM in WT cells. Depicted is the fraction of PM versus total labeling per cell. (*D*) Single-particle tracking PALM analysis of ΔNC-Gag-mEOS2 in WT cells expressing pNL43ΔPolΔNC-Gag-mEOS2. The histogram shows the distribution of lateral diffusion coefficients of single ΔNC-Gag molecules (1,526 tracks) within Gag complexes acquired from 10 cells (green bar), plotted together with the distribution of diffusion coefficients of the WT Gag at the PM of the WT cells (gray bar) as in Fig. 1*G*. (*Inset*) Mean ± SEM diffusion coefficients for the three conditions. Note that ΔNC-Gag exhibited the fastest diffusion rate. (*E*) Schematic model of how miRNA could interfere with Gag assembly at the PM, based on spt-PALM analysis. (*F* and *G*) Immunoprecipitation (IP) of miRNA-Gag complexes. miR^+ cells were transfected with either pNL43ΔPolΔEnvGag or pNL43ΔPolΔNC-Gag. At 48 h posttransfection, the cells were lysed and immunoprecipitation of Gag or ΔNC-Gag was performed. (*F*) Representative Western blot image of Gag and ΔNC-Gag proteins immunoprecipated from the miR^+ cells. (*G*) The presence of miR-146a in the IP material was confirmed by qRT-PCR, normalized to the mean ΔNC-Gag protein (*E*) input (1:7.5). All data are represented as mean ± SD of at least three replicate experiments unless otherwise noted. (Scale bar, 10 μm.)

The above results suggested that Gag dynamics at the PM change depending on whether or not Gag interacts with viral RNA (Fig. 2*E*). Under conditions where Gag efficiently interacts with viral RNA (i.e., Fig. 2*E*, *Left*, WT Gag), Gag–RNA complexes wind up into tight clusters that are immobile. When Gag cannot interact with RNA (i.e., Fig. 2*E*, *Right*, ΔNC-Gag), the protein freely diffuses at the PM without clustering. When Gag–RNA interactions are partially disrupted by overexpression of miRNA (i.e., Fig. 2*E*, *Center*, WT Gag + miRNA), Gag–RNA complexes do not wind up into tight clusters and exhibit an intermediate mobility between ΔNC-Gag and Gag in WT cells. Evidence that exogenous miRNAs in miRNA-overexpressing cells in fact bind to Gag came from RNA-immunoprecipitation experiments demonstrating a binding interaction between Gag and miRNA-146a (Fig. 2 *F* and *G*). The quantity of miRNA-146a retrieved by immunoprecipitating Gag from miR^+ cells expressing WT Gag was much greater than that observed during immunoprecipitation of ΔNC-Gag from miR^+ cells expressing ΔNC-Gag, suggesting miRNA-146a binds to Gag via the protein's NC domain.

The observed effect of miRNA overexpression on the dynamics of Gag at the PM (i.e., reduced clustering of Gag and decreased budding of Gag particles from the PM), prompted us to examine the fate of Gag in miR^+ cells. Fluorescence imaging showed that large vacuoles enriched in Gag were formed over time (Fig. 3*A*, arrow). These vacuoles ranged in size from 1 to 10 μm in diameter. Gag proteins increasingly appeared in such vacuoles in miR^+ cells with time, reaching a plateau in which 50.3 ± 4.6% of the cells contained one or more Gag-positive vacuoles at the end of 48 h (Fig. 3*B*). Similar results were observed for miR^+888 cells (*SI Appendix*, Fig. S8). By contrast, only 14.3 ± 6.9% of WT cells and 14.1 ± 4.3% of empty vector control cells expressing Gag contained such vacuoles at the end of 48 h (*SI Appendix*, Fig. S9). Large vacuoles were not present in miR^+ or miR^+888 cells that were not expressing Gag, suggesting that the vacuoles were induced by Gag expression. Processing of Gag in cells containing exogenous miRNA was decreased relative to WT cells, as expected if Gag assembly at the PM is impaired (*SI Appendix*, Fig. S10). Thus, under conditions of improperly assembled Gag complexes at the PM in miRNA-overexpressing cells, Gag redistributes into large intracellular vacuoles.

Few, if any, Gag-containing vacuoles formed in miR^+ cells expressing ΔNC-Gag (Fig. 2*B*). This suggested that vacuole formation was dependent on miRNA–Gag interactions. To further examine this dependence, we expressed a Gag mutant whose NC domain was replaced with an isoleucine-zipper domain (i.e., Gag-ZiL), expressed using the pNL4-3-ZiLΔPolΔEnv construct. Expressed Gag-ZiL molecules do not bind RNA because they lack the NC domain of Gag. Because of their leucine-zipper domain, however, they can still multimerize and form virus-like particles (19). The Gag-ZiL particles are noninfectious, lacking detectable viral RNA (*SI Appendix, Gag-ZiL and ΔNC-Gag*). We found that miR^+ cells expressing Gag-ZiL had significantly reduced numbers of induced vacuoles (~13% of cells observed 48 h posttransfection) relative to that seen in miR^+ cells expressing Gag (Fig. 3*C*). In addition, the numbers of Gag-ZiL particles released by WT or miR^+ cells expressing Gag-ZiL were similar (*SI Appendix*, Fig. S11). This indicated that miRNAs do not affect multimerization and budding of Gag-ZiL, which requires only Gag-ZiL's isoleucine-zipper domain. Therefore,

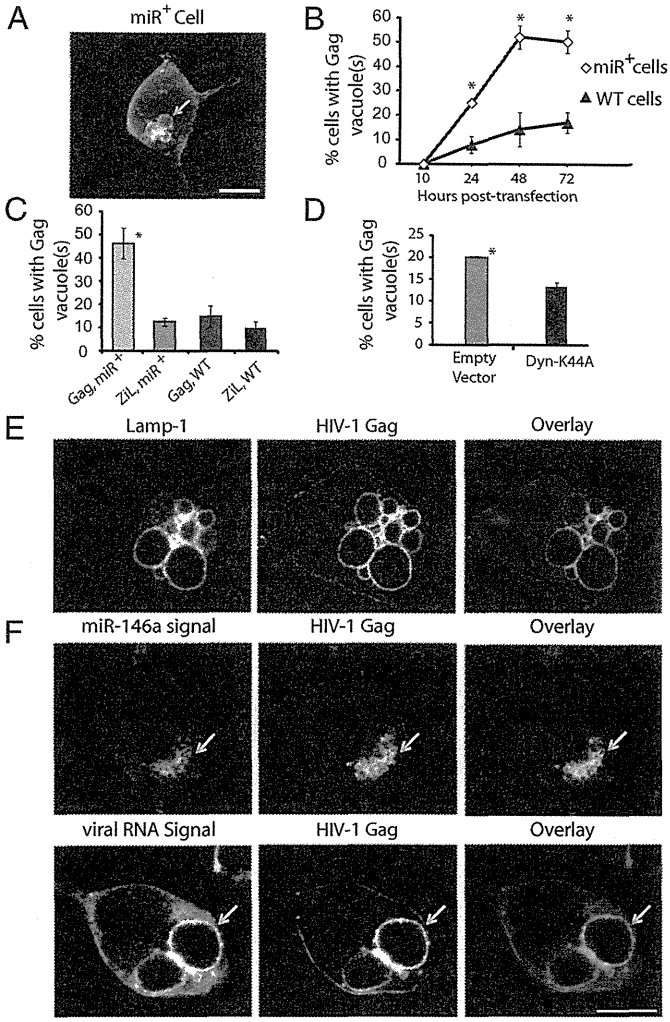

Fig. 3. miRNA–Gag interactions drive the internalization of Gag complexes at the PM, leading to formation of large, Lamp1-enriched intracellular vacuoles. (*A*) Representative images of Gag expressed in miR$^+$ cells through pNL43ΔPolΔEnvGag-GFP transfection. Note the appearance of large intracellular vacuoles enriched in Gag. (*B*) Percentage of cells having large intracellular vacuoles enriched in Gag as a function of time after transfection. (*C*) Percentage of Gag (expressed via pNL43ΔPolΔEnv) or Gag-ZiL–positive vacuoles (detected by immunofluorescence with anti-p24 antibodies) seen in cells expressing Gag or Gag-ZiL in WT or miR$^+$ cells. (*D*) Reduction in vacuole formation in response to dynamin-K44A, a dominant-negative mutant that inhibits dynamin-dependent endocytosis. (*E*) miR$^+$ cells expressing pNL43ΔPolΔEnvGag-GFP were fixed and immunofluorescently labeled with anti–Lamp-1 antibodies to stain lysosomes. Lamp-1 distribution colocalized with Gag-GFP in large intracellular vacuoles, identifying these structures as lysosomes. Nucleus, blue (stained with DAPI). (*F*) Representative images of miR-146a or unspliced HIV-1 RNA (detected by FISH) and Gag (detected by Gag-GFP) in WT and miR$^+$ cells transfected with pNL43ΔPolΔEnvGag-GFP. Arrows point to the vacuoles. All data are represented as mean ± SD of at least three replicate experiments. Each replicate experiment is performed by visually examining at least 200 transfected cells. (Scale bar, 10 μm.)

the increased production of large, Gag-enriched vacuoles in miR$^+$ cells requires interactions between miRNA and Gag's NC domain.

To clarify the nature of the Gag-enriched vacuoles seen in miRNA-overexpressing cells, we tested if they arose by endocytosis of Gag from the PM. Coexpression of HIV-1 constructs and mutant dynamin (i.e., Dyn-K44A, which inhibits severing of clathrin-coated vesicles) in miR$^+$ cells led to a reduction in vacuole formation (Fig. 3*D*). This indicated that dynamin-dependent endocytosis facilitates Gag accumulation within vacuoles. Immunofluorescent labeling with lysosomal-associated membrane protein (LAMP)-specific antibodies identified the vacuoles as being late endosomal or lysosomal compartments (*SI Appendix*, Fig. S12 and Fig. 3*E*). Treatment with the lysosomal protease inhibitor leupeptin led to Gag accumulation inside the vacuoles rather than just at their membrane periphery (*SI Appendix*, Fig. S13). This suggested that Gag is normally destroyed after being transferred inside the vacuole. FISH experiments further showed that HIV-1 RNA and the miRNA-146a were both enriched within Gag vacuoles, colocalizing with Gag (Fig. 3*F* and *SI Appendix*, Fig. S14). Overall, these results revealed that Gag-enriched, lysosome-related vacuoles are formed through endocytosis of Gag complexes containing not only Gag but also HIV-1 RNA and miRNA. This explains the overall reduced levels of Gag at the PM of miRNA-overexpressing cells.

To assess what levels of miRNAs are required to disrupt Gag assembly and cause Gag delivery to vacuoles, we quantified endogenous miRNA levels relative to exogenous miRNA (i.e., miRNA-146a) levels using quantitative RT-PCR (qRT-PCR) analysis (Fig. 4*A*). miRNA-146a levels were similar to those of several highly abundant endogenous miRNAs (Fig. 4*A*). This prompted us to examine whether Gag could bind to endogenous miRNAs, not just exogenous miRNAs. Supporting this hypothesis, Gag-miRNA immunoprecipitation experiments revealed that in addition to miRNA-146a, other host miRNA species coimmunoprecipitated with Gag, including miR-17, miR-19, and miR-16 (Fig. 4*B*), consistent with previous work showing that Gag can nonspecifically bind to nucleic acids (20). Nonetheless, there was a nearly threefold enrichment of miRNA-146a relative to that of the retrieved endogenous miRNAs (i.e., miR-16) in the immunoprecipitate. The similar expression levels of endogenous and exogenous miRNAs within cells, yet significantly different levels in the immunoprecipitates, raised the question of why Gag would preferentially bind to exogenous over endogenous miRNAs.

It is thought that most endogenous miRNAs within cells are bound to RNA-induced silencing complexes (RISCs), forming miRNA-RISCs that regulate the expression of a variety of host cellular genes (21). Therefore, most endogenous miRNAs within cells should be unable to interact with Gag at the PM to interfere with Gag assembly. By contrast, exogenous miRNAs that we introduced in HEK293 cells with no known mRNA targets would be available to bind Gag and interfere with Gag assembly. To test this idea, plasmid constructs encoding target mRNAs for miRNA-146a were coexpressed with Gag-GFP–expressing HIV-1 proviral clones in miR$^+$ cells. Our assumption was that if our hypothesis was correct, then in these cells fewer Gag proteins should be internalized and delivered into vacuoles because miRNA-146a would interact with the expressed target mRNA within silencing machinery rather than with Gag at the PM. Consistent with this possibility, we found that fewer Gag vacuoles formed in miR$^+$ cells expressing Gag plus the target mRNA for miRNA-146a compared with miR$^+$ cells expressing Gag plus the empty vector control (Fig. 4*C*). Exogenous miRNAs, therefore, may interact with Gag more efficiently than endogenous miRNAs because they lack mRNA targets.

The above findings led us to investigate whether depletion of Argonaute 2 (Ago2), which binds miRNAs to form RISCs, makes the endogenous miRNAs available for interacting with Gag to disrupt viral assembly. Supporting this possibility, knockdown of Ago2 led to increased numbers of Gag-enriched intracellular vacuoles and decreased viral particle formation in WT HEK293 cells expressing Gag (Fig. 4*D* and *SI Appendix*, Fig. S15). The effects were analogous to those seen in Gag-expressing cells overexpressing foreign miRNAs. Gag-enriched intracellular vacuoles were also seen in Gag-expressing WT HEK293T and HeLa cells after knockdown of Ago2 (*SI Appendix*, Fig. S16). Endogenous miRNAs, therefore, may also interact with Gag to disrupt Gag assembly when not packaged with RISCs.

To test this idea further, we depleted proteins necessary for the biogenesis of miRNAs, including Dicer or Drosha (22). We reasoned that in cells depleted of either Dicer or Drosha, there would be few miRNAs available to bind to Gag and disrupt viral assembly. Supporting this hypothesis, partial knockdown of Dicer or Drosha led to reduced numbers of Gag-enriched intracellular vacuoles but enhanced viral particle formation in WT HEK293 cells expressing Gag (Fig. 4 *E* and *F*). This supported the idea that any miRNA when not mediating RNAi activities can obstruct viral assembly via miRNA–Gag interactions.

In summary, our results suggest that miRNA, when unbound to silencing machinery, can bind to Gag proteins and disrupt Gag clustering into viral particles at the PM (Fig. 4*G*). Improperly assembled Gag complexes so formed undergo enhanced endocytic delivery to lysosomes. This effect of miRNA on Gag assembly is more pronounced in cells that have miRNAs not engaged in RNAi activities. These findings linking miRNA with Gag physiology have significant implications for understanding how cells modulate HIV-1 infection. Gene expression is increasingly known to occur stochastically, with cell-to-cell variations in mRNA and protein levels (23–27). Moreover, transcription rates often exhibit pulsatile variations (23–27). Production of miRNAs may therefore sometimes be out of sync with mRNA transcription, leading to buildup of miRNAs not bound to mRNA or RISCs. The RISC-free miRNAs could then become potent inhibitors of viral production and regulators of Gag physiology. In this context, expression of total miRNAs may play an equal if not a more important role than specific miRNAs in regulating HIV-1 biogenesis. Given the ever-growing development of antiviral agents designed to target HIV-1 assembly, our results suggest the possibility of manipulating total expression levels of host miRNAs to combat HIV-1 transmission and infectivity.

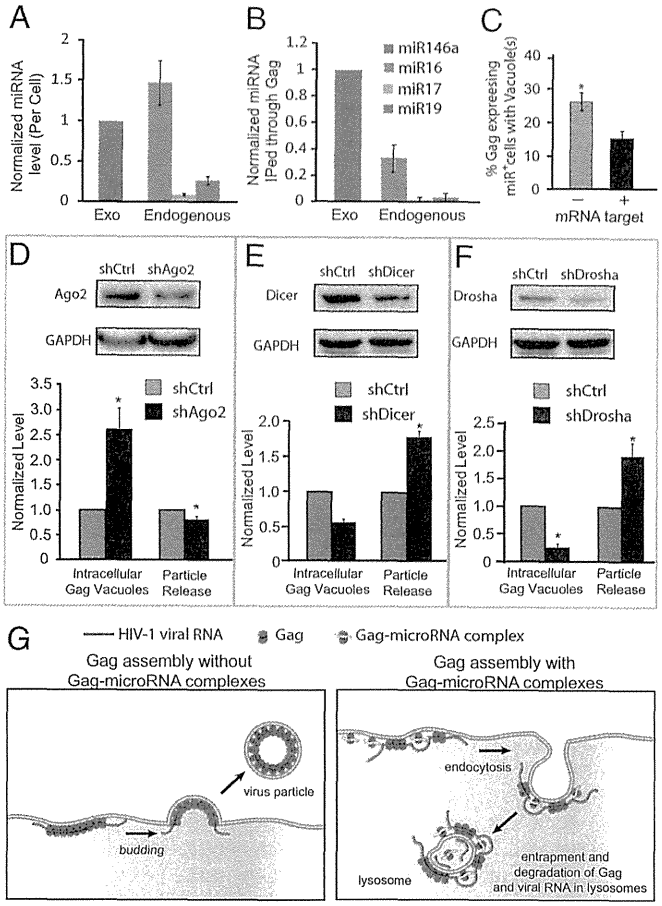

Fig. 4. miRNAs disrupt Gag assembly when they do not participate in RNAi activity. (*A*) Expression levels of the exogenous (exo) miR-146a and endogenous miR-16, -17, and -19 in the miR$^+$ cells. Levels determined by qRT-PCR were normalized to the miR-146a level per cell. Note that miR-146a and miR-16 were expressed at similar levels. (*B*) Levels of the miR-146a and the endogenous miR-16, -17, and -19 retrieved by immunoprecipitating Gag from the miR$^+$ cells. Note that significantly more miR-146a than miR-16 is retrieved by IP of Gag. (*C*) Addition of mRNA targets for the miR-146a reduced vacuole formation. miR$^+$ cells were cotransfected with pNL43ΔPolΔEnv and the mRNA target or empty plasmids (*Materials and Methods* for construct details). At 24 h posttransfection, percentage of Gag expressing miR$^+$ cells containing at least one vacuole were assayed by fluorescence microscopy. (*D–F*) The effect of knockdown of Ago2, Dicer, and Drosha on vacuole formation and Gag particle release. shRNA-Ago2, shRNA-Dicer, shRNA-Drosha (or shRNA-ctrl, a control shRNA) and pNL43ΔPolΔEnvGag-GFP were cotransfected in WT HEK293 cells. At 24 h posttransfection, Western blot was performed to assess the knockdown efficiency. Ago2 shRNA treatment reduced the levels of Ago2 by ~50%, whereas Dicer shRNA and Drosha shRNA treatments reduced the Dicer and Drosha levels by 23% and 20%, respectively. Vacuoles and particle release were assayed by fluorescence microscopy as described in *Materials and Methods*. All data are represented as mean ± SD of at least three replicate experiments. Results were normalized to the number of vacuoles observed in the cells cotransfected with shRNA-ctrl. For the vacuole analysis in *C–F*, each replicate experiment is performed by visually examining at least 150 transfected cells. (*G*) Schematic model of Gag–miRNA complexes interfering with Gag assembly at the plasma membrane. In the absence of Gag–miRNA complexes, Gag and the HIV-1 viral RNA form stable complexes at the PM, resulting in viral budding. When Gag–miRNA complexes are present within the viral RNA-mediated assembling complexes, they interfere with proper Gag assembly, resulting in internal vacuole formation.

Materials and Methods

Cell Culture. Human embryonic kidney 293 (293), 293T, HeLa cell lines (American Type Culture Collection), the HIV reporter cell line TZM-bl [National Institutes of Health (NIH) AIDS Research and Reference Reagent Program, Germantown, MD], and miRNA-overexpressing cells (miR$^+$ and miR$^+$888) were cultured in Dulbecco's modified eagle medium (DMEM; Mediatech), supplemented with 10% (vol/vol) FBS (Invitrogen) at 37 °C, 5% (vol/vol) CO_2, and 90% relative humidity. All experiments were performed with cells at passage numbers between 10 and 25.

miRNA Expression Plasmids. Precursor miR-146a expression plasmid (backbone pBApo-CMV Neo) was described previously (28). Precursor miR888 expression vector was constructed by PCR amplification of the human genomic DNA with forward primer ACCTGCGGGATCCCTTCTGGTCCTGGCAATCAT and reverse primer ACTGCTAAGCTTACCAGTCTGAGGACCACCAC. The PCR product was then inserted into pBApo-CMV Neo digested with BamH1 and HindIII. The neo-resistant miRNA constructs also served as the PCR templates for constructing hygromycin-resistant precursor miRNA expression vectors. For the hygro precursor miR-146a vector, forward and reverse primers were ACCTGCGCTAGCTTTACAGGGCTGGGACAGG and ACTGCTGCGGCCGCAAGCTCTTCAGCAGACTGAAAA. For the hygro precursor-miR-888 vector, the forward and reverse primers were ACCTGCGCTAGCCTTCTGGTCCTGGCAATCAT and ACTGCTGCGGCCGCACCAGTCTGAGGACCACCAC, respectively. The resulting PCR products were then inserted into the NheI and NotI sites of Hyg-N1, constructed by excising out the sequences encoding DsRed-Monomer from the pDsRed-Monomer-Hyg-N1 vector with NheI and NotI. The functionality of all precursor miR constructs were confirmed by miR-reporter assays (see below).

miR-Reporter Constructs. The construction of miRNA reporter construct for miR-146a was described previously (28). miRNA reporter construct for miR-888 was constructed similarly by introducing multiple tandem repeats of binding sites perfectly complementary to miR888 into the NotI site of psiCHECK2 (Promega). For the miR888 reporter construct, the following sequences were inserted: GCGGCCGCTGACTGACAGCTTTTTGAGTAAAGAATTCTTTGACTGACAGCTTTTTGAGTAAAGAATTCTTTGACTGACAGCTTTTTGAGTAGCGGCCGC. (The underlined sequence is complementary to miR888.)

Viral Constructs. The pNL43 proviral construct (29) was used to construct other pNL43 derivatives used in this study. These constructs including

pNL43ΔPolΔEnv, pNL43ΔPolΔEnvGag-GFP, pNL43ΔPolΔEnvGag-mEOS2, pNL43ΔNCΔPolΔEnv, pNL43ΔNCΔPolΔEnvGag-GFP, pNL43ΔNCΔPolΔEnvGag-GFP, ΔNCΔPolGag-mEOS2, and pNL43ZiLΔPolΔEnv are described below.

The pNL43ΔPolΔEnv was constructed by subcloning the SpeI–SalI and SalI–BamHI regions from pNL43 into pBluescript (SK+), deleting the BclI–NsiI and NsiI–BglII regions from the *pol* and *env* genes, respectively, and inserting the resulting SpeI–SalI and SalI–BamHI regions back to pNL43. The pNL43ΔPolΔEnvGag-GFP was constructed by inserting GFP from pNL4-3/iGFP [a kind gift from Benjamin Chen (Mount Sinai School of Medicine, New York)] into the BssHII–SpeI region of pNL43ΔPolΔEnv. The pNL43ΔPolΔEnvGag-mEOS2 was constructed by amplification of pCMV-mEosFP2-C1 with BsiE-AclI flanking primers. The amplified PCR products were subcloned into pBluescript (SK+) containing the HindIII–SpeI region of pNL43, where the synthetic cleavage site at the C terminus of the matrix domain and the cloning sites (BstBI and PacI) were introduced. The inserted sequences are indicated in uppercase in the following: gtc*TCGCAGAACTATCCAATTGTACAA*TTCGAAGGTTAATTAAgccaa (the sequences for the synthetic cleavage site are in italics and the restriction sites are underlined). The resulting partial fluorescent proteins (FPs) were cloned into pNL43ΔPolΔEnv by insertion into the BssHII–SpeI site. The pNL43ΔPolΔEnvΔNC was made by subcloning the SpeI–EcoRI region from pNL43 ΔNC [a kind gift from David Ott (National Cancer Institute, Frederick, MD)], deleting the BclI–NsiI fragment of the Pol region, and cloning into pNL43ΔPolΔEnv by insertion into the SpeI–EcoRI site. The pNL43ΔPolΔEnvΔNC-Gag-GFP was constructed by insertion of the SpeI–EcoRI site from pNL43 ΔPolΔEnvΔNC into pNL43-ΔPolΔEnvGag-GFP. The pNL43ΔPolΔNC-Gag-mEOS2 was constructed by insertion of the SpeI–EcoRI fragment from pNL43ΔPolΔEnvΔNC into pNL43/imEosFP2. The pNL4-3 Zil ΔPolΔEnv construct was made by amplifying the SpeI–ApaI region of Zil-p1p6 (30) and cloning into pNL43ΔPolΔEnv.

shRNA Constructs. pTER-shAgo2 and pTER-shDicer plasmids were kind gifts from P. Svoboda (Friedrich Miescher Institute for Biomedical Research, Basel, Switzerland). The shRNA Drosha plasmid was a kind gift from Tyler Jacks (Massachusetts Institute of Technology, Cambridge, MA). To construct the pTER-shCtrl plasmid, the sequences encoding shAgo2 in the pTER-shAgo2 were replaced with sequences AAGAGATAGTTGCGGACAATCTGACTTTTTT using BglII and HindIII restriction sites.

Transfection. Transfection was performed with Fugene 6 (Promega) unless otherwise noted as per manufacturer's protocol when cells reached 50–70% confluency. For fluorescent microscopic studies where FPs were used, cells seeded on clean coverslips or labtek chambers (Nunc) were transfected with a mixture containing both FP-tagged and untagged PNL43 derivative constructs at a 1:3 ratio. This is to avoid potential morphological defects in Gag assembly caused by expressing Gag tagged with FP alone. For shRNA knockdown studies, equal amounts of shRNA constructs and pNL43 derivative constructs were transfected.

Establishment of Cell Lines Stably Expressing Exogenous miRNAs. HEK293 cell lines stably expressing hsa-miR-146a or hsa-miR888 were generated by two successive selections using miRNA expressing plasmids with neomycin- and hygromycin-resistant genes. This allowed the establishment of stable cell lines with high miRNA activity. First, cells transfected with miRNA-expressing vectors (derived from neomycin-resistant plasmids) were cultured in media containing 1–2 mg/mL geneticin. After 2 wk, single colonies were isolated, maintained in 0.5–1 mg/mL geneticin for 3 wk, and thereafter cultured without geneticin. The clone that exhibits the highest miRNA activity (as determined by miR-reporter assay) was further used to generate double stable cell lines by further transfecting it with hygromycin-resistant plasmids containing hsa-miR-146a or hsa-miR888. After selection in culture media containing 20–60 ng/mL hygromycin, single colonies were isolated and maintained in 10–30 ng/mL hygromycin for 3 wk and thereafter cultured without any antibiotics. The colony with the highest microRNA activity was selected for further studies.

Assessment of Total Gag Expression Levels. Radioimmunoprecipitation assays were carried out as previously described (31). Briefly, WT HEK293 and miRNA-expressing cells were transfected with the HIV-1 molecular clone pNL4-3 by using Lipofectamine 2000 reagent (Invitrogen). At 24 h posttransfection, HIV-1–expressing cells were starved in [^{35}S]Met/Cys-free medium (MPBio) for 30 min and metabolically labeled for 2 h with [^{35}S]Met/Cys-Promix (Perkin-Elmer). Virions released into the medium were collected by ultracentrifugation at 100,000 × *g* for 45–60 min. Cell and virus lysates were immunoprecipitated with pooled Ig from HIV-1–infected patients (HIV-Ig) obtained from the NIH AIDS Research and Reference Reagent Program. Immunoprecipitated proteins were separated on 12% (wt/vol) acrylamide gels by SDS/PAGE, exposed to a phosphorimager plate (Fuji), and quantified by Quantity One software (Bio-Rad). In general, Gag detected in the supernatant represents only a minor fraction of total Gag labeled during a 2-h labeling period; therefore, virion-associated Gag is neglected for the measurements of total Gag expression levels. In some measurements, Gag expression was divided by the Envelope (Env) expression to correct for variations in transfection efficiency (*SI Appendix*, Fig. S17).

Infectivity Assay. For luciferase-based, single-cycle infectivity assays, viral supernatant from WT cells and miRNA-expressing derivatives transfected with pNL4-3 were used to infect the CD4$^+$/CXCR4$^+$/CCR5$^+$ HeLa cell derivative TZM-bl (obtained from J. Kappes and X. Wu through the AIDS Research and Reference Reagent Program) as previously described (32). Infection was carried out over a range of inputs from 1 to 10 μL of viral supernatant collected from the WT or miRNA-overexpressng cells for 2 h. At 48 h post-infection, cells were lysed and infectivity was measured using the Britelite Plus (Perkin-Elmer) Luciferase Reporter Gene Assay system. Percent infectivity was normalized based on reverse transcriptase (RT) activity. Datasets in the linear range of sensitivity were used as a means to assess the effect of miRNAs on virus infectivity.

miRNA Functional Analysis. Cells were plated at 50,000 cells per well in a 24-well tissue culture plate overnight. The next day, cells were transfected with 0.5 μg miR-reporter plasmids using Fugene 6 as per manufacturer's instructions. Twenty-four hours posttransfection, the samples were harvested and luciferase signals were measured using the Dual Luciferase Reporter Assay kit (Promega) following the manufacturer's instructions. Signals were acquired on a luminometer (LMaxII, Molecular Devices), and the ratio between the Renilla and the firefly luciferase internal control was used to quantify the repression efficiency indicative of the activity of the microRNAs.

Fluorescent Microscopy. Confocal imaging was performed with a Marianas spinning disk (Intelligent Imaging Innovations) attached to a Zeiss Observer. Z1 microscope (Carl Zeiss) equipped with a 63× and a 100× Plan Apochromat 1.4 NA (Carl Zeiss) objective lens or a Zeiss 710 with a 63× oil-immersion objective. Maximum-intensity projection images were constructed using ImageJ. TIRF imaging was performed on an Elyra PS.1 system (Carl Zeiss) using a 100× 1.46 NA objective and a 488-nm excitation laser (100 mW).

PALM Acquisition. Eighteen- or 25-mm 1.5 thickness coverslips (Warner Instruments) were cleaned as previously described (33). Cells were grown on cleaned coverslips coated with fibronectin (2 μg × mL^{-1} in PBS, pH 7.4; Sigma) and transfected with pNL4-3ΔPΔE and pNL4-3-imEOS2-ΔPΔE as described above. For spt-PALM experiments, cells were placed in phenol red free DMEM containing 25 mM Hepes and 1% FBS and imaged at 37 °C. Imaging was performed on either a custom Olympus IX81 microscope with modified TIRF illuminator port and 60× 1.45 NA PlanApoN objective (Olympus) or a commercial TIRF Elyra PS.1 system using a 100× 1.46 NA objective (Carl Zeiss). Fluorescence emission was detected using an EM-CCD camera (Andor Technology, DU-897). Images were obtained by spontaneous photoconversion of mEOS2 probes using 500–900 μW of 561 nm light measured from the rear aperture of the objective. Upon significant depletion of mEOS2, 405 nm light was used at 5–10 μW in 500-ms pulses on intervals of 1–3 min to recover additional tracks. Images were acquired at 20 frames per second.

Spt-PALM Analysis. Single molecules were localized using either a previously described algorithm written in IDL (Research Systems) (17) or commercially available software (Elyra PS.1 system, Carl Zeiss). Peaks identified in each frame were fit with a cylindrically symmetric Gaussian point spread function. The average localization precision of the peaks ranged between 20 and 35 nm. PALM images were collected under conditions where average distance between peaks in a single frame was substantially larger than the maximum distance that a single molecule is expected to move between two consecutive frames. The rest of the analysis was performed using code custom written in MATLAB (Mathworks). Single molecule peaks localized to better than 25 nm were only used for the final analysis. For single molecules diffusing with an average diffusion coefficient of 0.1 μm^2/s (previously reported diffusion coefficient of Gag), 99% of molecules are expected to move less than 300 nm between two consecutive frames. Peaks present in consecutive frames within a distance of 300 nm were assigned to the same trajectory, representing the successive positions of the same molecule. Trajectories containing at least 15 steps were selected for calculating the average short-term diffusion coefficient (D_{eff}). The mean square displacement (MSD) corresponding to different time lags ($\Delta\tau$) was calculated by averaging the MSD over overlapping time windows. Finally, the D_{eff} of each trajectory was

obtained from a linear fitting of MSD vs. $\Delta\tau$ plot, using the first five time lags ($0 < \Delta\tau < 250$ ms).

Cluster Analysis. The single molecule localizations (with localization precision 30 nm or less) from all of the acquisition frames of a PALM time series of live cell (10,000 frames acquired over 8.3 min at 20 frames per second) were combined to form a composite, superresolution image. Hoshen–Kopelman algorithm (34)-based cluster analysis was performed on this composite image to identify individual clusters of Gag molecules. Briefly, Gag molecules with neighboring molecules within a distance of 300 nm were identified and grouped together with all of the shared neighbors into the same cluster. From the set of clusters obtained from this operation, only clusters with a radius less than or equal to 150 nm and density greater than three times the average density of Gag over the plasma membrane were considered as Gag platforms (nascent viral buds) arising from oligomerization of Gag at the plasma membrane. Next, the size of each cluster was determined by calculating the convex hull (the smallest convex set) for the set of molecules belonging to the cluster. The area of the convex hull and the radius of a circle of equivalent area (as the convex hull) were used as estimates of cluster area and cluster radius, respectively. The density of Gag-mEos2 within the convex hull was normalized with respect to the average density of Gag-mEos2 over the entire plasma membrane of the cell to obtain the cluster density.

Quantification of Particle Release. Supernatant containing particles encapsidating Gag and the Gag-GFP were harvested 48 h posttransfecton. Cell debris and large aggregates were removed by centrifugation at 200 × *g* for 10 min followed by filtration through a 0.45-μm filter. Subsequently, an aliquot of the purified supernatant was incubated on a polylysine-coated coverslip at room temperature for 1 h before being imaged and/or subjected to fluorescent in situ hybridization according to procedures below. All images were processed by setting an appropriate intensity threshold in the GFP channel to obtain a good contrast. The same threshold setting was used for an entire dataset, which included at least 50 unique fields of view. Images were analyzed using the "analyze particles" command on NIH ImageJ.

Fluorescent in Situ Hybridization of HIV-1 Viral RNA. Cells were fixed in PBS solution containing 4% (wt/vol) paraformaldehyde for 30 min at room temperature, washed with 1× PBS, and permeabilized at 4 °C in 70% (vol/vol) ethanol overnight. A pool of 48 oligonucleotides (listed in *SI Appendix*, Table S1), each labeled with a single Quasar 670 dye on the 3′ end and complementary to a different region of the target HIV-1 mRNA, were designed using custom FISH design software and manufactured by Biosearch Technologies. FISHs were performed according to the manufacturer's protocol with slight modifications. In brief, after overnight permeabilization in 70% ethanol, the cells were washed with wash buffer [2× SSC, 10% (vol/vol) formamide] and then incubated in hybridization buffer [10% (wt/vol) dextran sulfate, 2× SSC, 10% (vol/vol) formamide] containing 500-nM probes for 4 h at 37 °C in a humidified chamber. Slides were washed with wash buffer to remove the unbound probes.

MicroRNA-Fluorescent in Situ Hybridization. After the fixation and permeabilization step as described above, the cells were wash once with 0.2% (wt/vol) glycine/TBS, twice with 1× TBS, and then crosslinked with l-ethyl-3-(3–dimethylaminopropyl) carbodiimide (EDC) similar to the procedure previously described (35). In brief, cells were incubated twice for 10 min in a freshly prepared solution containing 0.13 M 1-methylimidazole, 300 mM NaCl, pH 8.0 adjusted with HCl. Then 0.16 M EDC (Pierce) was added to the cells and incubated for 1–2 h at room temperature. Before probe hybridization, the slides were washed in 0.2% (wt/vol) glycine/TBS, 1× TBS, and dehydrated in 70% ethanol followed by 99% (vol/vol) ethanol. Hybridization was carried out in hybridization buffer (Exiqon) containing 100 nM of the antisense miR-146a or scrambled locked nucleic acid probes (Exiqon) in a humidified chamber at 55 °C overnight. After stringent washes in 5× SSC, 1× SSC, and 0.2× SSC, the slides were blocked in 1× blocking solution (1% blocking reagent, 100 mM maleic acid, 150 mM NaCl, PH 7.5) (Roche) for 15 min and then incubated with anti-Dig-POD (1:500) in the blocking solution overnight at 4 °C. After washing the slides with wash buffer (0.1 M Tris·HCl, 0.15 M NaCl, 0.05% Tween20 pH 7.5), the samples were subject to Cy5-plus tyramide (1:100 dilution of stock solution in 1X Plus Amplification Diluent) using the TSA plus amplification system (Perkin-Elmer) according to the manufacturer's protocol.

Quantitative RT-PCR of miRNA. Total RNA was isolated from 10^6 cells using TRIzol according to the manufacturer's instructions. RNA concentrations were determined using a Cary100 UV-Vis spectrophotometer (Varian). cDNA synthesis was performed in parallel with RNA standards using the Taqman microRNA Reverse Transcription kit according to the manufacturer's instructions. RNA oligonucleotides with the same sequence as matured miRNA (miRNA-16, miRNA-17, miR-19, miR146a, and miR888) (Integrated DNA Technologies) were used as the standards for miRNA quantification. All PCR experiments were performed using Taqman gene expression assays on an ABI StepOnePlus Real-Time PCR system (Applied Biosystems) according to the manufacturer's instructions.

Immunoprecipitation of MicroRNA–Gag Complexes. Immunoprecipitation of microRNA–Gag complexes was performed according to a procedure described previously with modifications (36). In brief, 1×10^7 cells were transiently transfected with 4 μg of pNL43ΔPolΔEnvGag or pNL43ΔPolΔEnvΔNC-Gag constructs. At 2 d posttransfection, cells were harvested in 500 μL of lysis buffer (100 mM KCl/5 mM MgCl2/10 mM Hepes, pH 7.05/0.5% Nonidet P-40/1 mM DTT/100). Following gentle mixing for 30 min at 4 °C, lysate was centrifuged at 16,000 × *g* for 30 min before being subjected to precleaning with proteinA-agarose beads for 1 h at 4 °C. A total of 500 μL of the precleaned lysates was recovered. HIV-Ig was added at 25 μg/mL of the recovered lysates. After overnight incubation with gentle mixing at 4 °C, 20 μL of 50% (vol/vol) protein-A agarose bead slurry was added to each sample and mixed for 4 h at 4 °C. The beads were then washed with lysis buffer with and without 1 M urea. A total of 50% of the sample was spun down at 16,000 × *g* for 20 min and the beads were resuspended in elution buffer and an aliquot was taken to determine the input of Gag or ΔNC-Gag by Western blot analysis. The other 50% of the sample was spun down at 16,000 × *g* for 20 min, resuspended, and incubated in polysome lysis buffer containing 0.1% SDS and 30 μg proteinase K at 50 °C for 30 min. Following phenol–chloroform extraction and ethanol precipitation, RNA was further purified from residual contaminants by lithium chloride precipitation. The purified RNA was subjected to cDNA synthesis and qRT-PCR analysis according to procedures described above.

Data Analysis. All experiments were repeated at least three times unless otherwise stated. Statistics were performed using one-way ANOVA with post hoc testing of pairwise comparisons using Fisher's protected least significant difference. Significant difference was taken at the $P < 0.05$ level.

ACKNOWLEDGMENTS. The authors thank Dr. Nobuyoshi Kosaka for providing the miR-146a and its reporter plasmids and the members of J.L.-S.'s laboratory for helpful discussions. This project was supported in part by the National Natural Science Foundation of China (Grant 81371613 to A.K.C.) and China's 1000 Young Talent Award program (A.K.C.).

1. Briggs JA, et al. (2004) The stoichiometry of Gag protein in HIV-1. *Nat Struct Mol Biol* 11(7):672–675.
2. De Guzman RN, et al. (1998) Structure of the HIV-1 nucleocapsid protein bound to the SL3 psi-RNA recognition element. *Science* 279(5349):384–388.
3. Amarasinghe GK, et al. (2000) NMR structure of the HIV-1 nucleocapsid protein bound to stem-loop SL2 of the psi-RNA packaging signal. Implications for genome recognition. *J Mol Biol* 301(2):491–511.
4. Campbell S, Vogt VM (1995) Self-assembly in vitro of purified CA-NC proteins from Rous sarcoma virus and human immunodeficiency virus type 1. *J Virol* 69(10): 6487–6497.
5. Muriaux D, Mirro J, Harvin D, Rein A (2001) RNA is a structural element in retrovirus particles. *Proc Natl Acad Sci USA* 98(9):5246–5251.
6. Jouvenet N, Simon SM, Bieniasz PD (2009) Imaging the interaction of HIV-1 genomes and Gag during assembly of individual viral particles. *Proc Natl Acad Sci USA* 106(45): 19114–19119.
7. Kutluay SB, Bieniasz PD (2010) Analysis of the initiating events in HIV-1 particle assembly and genome packaging. *PLoS Pathog* 6(11):e1001200.
8. Eiring AM, et al. (2010) miR-328 functions as an RNA decoy to modulate hnRNP E2 regulation of mRNA translation in leukemic blasts. *Cell* 140(5):652–665.
9. Fabbri M, et al. (2012) MicroRNAs bind to Toll-like receptors to induce prometastatic inflammatory response. *Proc Natl Acad Sci USA* 109(31):E2110–E2116.
10. Lehmann SM, et al. (2012) An unconventional role for miRNA: let-7 activates Toll-like receptor 7 and causes neurodegeneration. *Nat Neurosci* 15(6):827–835.
11. Vickers KC, Palmisano BT, Shoucri BM, Shamburek RD, Remaley AT (2011) MicroRNAs are transported in plasma and delivered to recipient cells by high-density lipoproteins. *Nat Cell Biol* 13(4):423–433.
12. Huang J, et al. (2007) Cellular microRNAs contribute to HIV-1 latency in resting primary CD4+ T lymphocytes. *Nat Med* 13(10):1241–1247.
13. Nathans R, et al. (2009) Cellular microRNA and P bodies modulate host-HIV-1 interactions. *Mol Cell* 34(6):696–709.

14. Sun G, et al. (2012) Interplay between HIV-1 infection and host microRNAs. *Nucleic Acids Res* 40(5):2181–2196.
15. Jouvenet N, Bieniasz PD, Simon SM (2008) Imaging the biogenesis of individual HIV-1 virions in live cells. *Nature* 454(7201):236–240.
16. Larson DR, Johnson MC, Webb WW, Vogt VM (2005) Visualization of retrovirus budding with correlated light and electron microscopy. *Proc Natl Acad Sci USA* 102(43):15453–15458.
17. Betzig E, et al. (2006) Imaging intracellular fluorescent proteins at nanometer resolution. *Science* 313(5793):1642–1645.
18. Manley S, et al. (2008) High-density mapping of single-molecule trajectories with photoactivated localization microscopy. *Nat Methods* 5(2):155–157.
19. Accola MA, Strack B, Göttlinger HG (2000) Efficient particle production by minimal Gag constructs which retain the carboxy-terminal domain of human immunodeficiency virus type 1 capsid-p2 and a late assembly domain. *J Virol* 74(12):5395–5402.
20. Rein A, Datta SA, Jones CP, Musier-Forsyth K (2011) Diverse interactions of retroviral Gag proteins with RNAs. *Trends Biochem Sci* 36(7):373–380.
21. Bartel DP (2004) MicroRNAs: Genomics, biogenesis, mechanism, and function. *Cell* 116(2):281–297.
22. Kim VN (2005) MicroRNA biogenesis: Coordinated cropping and dicing. *Nat Rev Mol Cell Biol* 6(5):376–385.
23. Muramoto T, et al. (2012) Live imaging of nascent RNA dynamics reveals distinct types of transcriptional pulse regulation. *Proc Natl Acad Sci USA* 109(19):7350–7355.
24. Raj A, van Oudenaarden A (2008) Nature, nurture, or chance: Stochastic gene expression and its consequences. *Cell* 135(2):216–226.
25. Chubb JR, Trcek T, Shenoy SM, Singer RH (2006) Transcriptional pulsing of a developmental gene. *Curr Biol* 16(10):1018–1025.
26. Larson DR, Singer RH, Zenklusen D (2009) A single molecule view of gene expression. *Trends Cell Biol* 19(11):630–637.
27. Raj A, Peskin CS, Tranchina D, Vargas DY, Tyagi S (2006) Stochastic mRNA synthesis in mammalian cells. *PLoS Biol* 4(10):e309.
28. Kosaka N, et al. (2010) Secretory mechanisms and intercellular transfer of microRNAs in living cells. *J Biol Chem* 285(23):17442–17452.
29. Adachi A, et al. (1986) Production of acquired immunodeficiency syndrome-associated retrovirus in human and nonhuman cells transfected with an infectious molecular clone. *J Virol* 59(2):284–291.
30. Popova E, Popov S, Göttlinger HG (2010) Human immunodeficiency virus type 1 nucleocapsid p1 confers ESCRT pathway dependence. *J Virol* 84(13):6590–6597.
31. Waki K, et al. (2012) Structural and functional insights into the HIV-1 maturation inhibitor binding pocket. *PLoS Pathog* 8(11):e1002997.
32. Waheed AA, et al. (2006) Inhibition of HIV-1 replication by amphotericin B methyl ester: Selection for resistant variants. *J Biol Chem* 281(39):28699–28711.
33. Sengupta P, et al. (2011) Probing protein heterogeneity in the plasma membrane using PALM and pair correlation analysis. *Nat Methods* 8(11):969–975.
34. Hoshen J, Kopelman R (1976) Percolation and cluster distribution. 1. Cluster multiple labeling technique and critical concentration algorithm. *Phys Rev B* 14(8):3438–3445.
35. Pena JT, et al. (2009) miRNA in situ hybridization in formaldehyde and EDC-fixed tissues. *Nat Methods* 6(2):139–141.
36. Peritz T, et al. (2006) Immunoprecipitation of mRNA-protein complexes. *Nat Protoc* 1(2):577–580.

STEM CELLS

CANCER STEM CELLS

Clinical Relevance and Therapeutic Significance of MicroRNA-133a Expression Profiles and Functions in Malignant Osteosarcoma-Initiating Cells

TOMOHIRO FUJIWARA,[a,b,c] TAKESHI KATSUDA,[a] KEITARO HAGIWARA,[a] NOBUYOSHI KOSAKA,[a] YUSUKE YOSHIOKA,[a] RYOU-U TAKAHASHI,[a] FUMITAKA TAKESHITA,[a] DAISUKE KUBOTA,[d] TADASHI KONDO,[d] HITOSHI ICHIKAWA,[e] AKIHIKO YOSHIDA,[f] EISUKE KOBAYASHI,[b] AKIRA KAWAI,[b] TOSHIFUMI OZAKI,[c] TAKAHIRO OCHIYA[a]

Key Words. Osteosarcoma • MicroRNA • Locked nucleic acid • Clinical translation

[a]Division of Molecular and Cellular Medicine, National Cancer Center Research Institute, Tokyo, Japan; [b]Department of Musculoskeletal Oncology, National Cancer Center Hospital, Tokyo, Japan; [c]Department of Orthopedic Surgery, Okayama University Graduate School of Medicine, Dentistry, and Pharmaceutical Sciences, Okayama, Japan; [d]Division of Pharmacoproteomics, National Cancer Center Research Institute, Tokyo, Japan; [e]Division of Genetics, National Cancer Center Research Institute, Tokyo, Japan; [f]Division of Pathology and Clinical Laboratories, National Cancer Center Hospital, Tokyo, Japan

Correspondence: Takahiro Ochiya, Ph.D., Division of Molecular and Cellular Medicine, National Cancer Center Research Institute, 5-1-1, Tsukiji, Chuo-ku, Tokyo 104-0045, Japan. Telephone: +81-3-3542-2511, ext. 4800; Fax: +81-3-5565-0727; e-mail: tochiya@ncc.go.jp

Received July 8, 2013; accepted for publication November 22, 2013; first published online in STEM CELLS *EXPRESS* December 19, 2013.

1066-5099/2014/$30.00/0

http://dx.doi.org/10.1002/stem.1618

ABSTRACT

Novel strategies against treatment-resistant tumor cells remain a challenging but promising therapeutic approach. Despite accumulated evidence suggesting the presence of highly malignant cell populations within tumors, the unsolved issues such as *in vivo* targeting and clinical relevance remain. Here, we report a preclinical trial based on the identified molecular mechanisms underlying osteosarcoma-initiating cells and their clinical relevance. We identified key microRNAs (miRNAs) that were deregulated in a highly malignant CD133^{high} population and found that miR-133a regulated the cell invasion that characterizes a lethal tumor phenotype. Silencing of miR-133a with locked nucleic acid (LNA) reduced cell invasion of this cell population, and systemic administration of LNA along with chemotherapy suppressed lung metastasis and prolonged the survival of osteosarcoma-bearing mice. Furthermore, in a clinical study, high expression levels of CD133 and miR-133a were significantly correlated with poor prognosis, whereas high expression levels of the four miR-133a target genes were correlated with good prognosis. Overall, silencing of miR-133a with concurrent chemotherapy would represent a novel strategy that targets multiple regulatory pathways associated with metastasis of the malignant cell population within osteosarcoma. STEM CELLS *2014;32:959–973*

INTRODUCTION

Sarcomas are distinctly heterogeneous tumors [1, 2]. Although the origin of sarcomas remains unknown, the overwhelming number of histopathological types and subtypes implies that sarcomas are a "stem cell malignancy" with multilineage differentiation abilities that result from dysregulated self-renewal [3]. The cancer stem cell theory, which states that a subset of cells within a tumor have stem-like phenotypes such as self-renewal and differentiation, has introduced a novel biological paradigm for many human tumors [4, 5]. These cancer stem cells (CSCs) or tumor-initiating cells (TICs) have been proposed to cause tumor recurrence and metastasis because of their lethal characteristics, including drug resistance, invasion, and tumorigenicity [6, 7]. Therefore, the development of TIC-targeted therapy would provide new hope for cancer patients, but these treatments have not reached the clinic.

Osteosarcoma is the most common primary bone malignancy [2, 8]. Along with the development of multiagent chemotherapy and surgical techniques including the concepts of surgical margins [9] and reconstruction [10], patient prognosis has gradually improved over the past 30 years. However, for patients who present with metastatic disease, the outcomes are far worse, with survival rates below 30%, within 5 years of diagnosis [11]. Furthermore, some cases present with distant metastases long after the initial treatment [12]. Considering these clinical characteristics and histopathological heterogeneity, emerging reports have implicated a role for osteosarcoma TICs [13–21]. However, the molecular mechanisms underlying the phenotypes of TICs and the importance of this population in clinical situations have not been elucidated. In this study, we focused on the multiple pathways within TICs in view of microRNA (miRNA) regulation.

Emerging evidence suggests that cancer initiation and progression involve miRNAs, which are small noncoding single-stranded RNAs of 20–22 nucleotides that negatively regulate gene expression at the post-transcriptional level through imperfect base paring with the 3′ untranslated region (UTR) of their target mRNA [22]. These miRNAs are

central to RNA interference (RNAi) [23]. The biogenesis of miRNAs involves a complex protein system, including members of the Argonaute family, Pol II-dependent transcription, and the RNase IIIs Drosha and Dicer [24]. Growing evidence suggests that miRNAs are involved in crucial biological processes, including development, differentiation, apoptosis, and proliferation [24]. Numerous profiling studies of miRNAs have revealed that deregulation of miRNA may contribute to many types of human diseases, including cancer. Depending on the target mRNAs that they regulate, miRNAs can function as tumor promoters or suppressors, regulating the maintenance and progression of cancers and TICs [25, 26]. In addition, miRNA expression profiles have been correlated with the tumor stage, progression, and prognosis of cancer patients [27, 28]. These findings indicate that miRNAs are critical regulators of tumor development and progression.

To date, the molecular mechanisms underlying the tumor-initiating phenotypes of osteosarcoma, their clinical correlations, and effective treatments against them have not been elucidated. In this study, we confirmed that the osteosarcoma $CD133^{high}$ cell population not only demonstrate a tumor-initiating phenotype but also show significant correlation with poor prognoses for osteosarcoma patients. In addition, we elucidated that miR-133a is a key regulator of cell invasion, which constitutes these malignant phenotypes of osteosarcoma, and that silencing of miR-133a with locked nucleic acid (LNA) inhibited osteosarcoma metastasis *in vivo* when applied with current chemotherapy. Furthermore, the expression of miR-133a and its target genes significantly correlated with the prognoses of osteosarcoma patients. Thus, our preclinical trial using LNA therapeutics may represent a novel strategy for osteosarcoma treatment through regulating multiple molecular pathways of the malignant cell population within osteosarcoma.

Materials and Methods

Osteosarcoma Cell Purification from Fresh Clinical Samples

Fresh human osteosarcoma samples were obtained in accordance with the ethical standards of the Institutional Committee on Human Experimentation from two patients who were undergoing diagnostic incisional biopsy from primary sites of osteosarcoma prior to receiving neoadjuvant chemotherapy at the National Cancer Center Hospital of Japan between October 2010 and June 2011. The osteosarcoma diagnosis and the histological subtypes were determined by certified pathologists. The surgical specimens were obtained at the time of resection and were received in the laboratory within 10 minutes, immediately mechanically disaggregated, digested with collagenase (Nitta Gelatin, Osaka, Japan, http://www.nitta-gelatin.co.jp) and washed twice with phosphate-buffered saline (PBS). The cells were cultured in Dulbecco's modified Eagle's medium (DMEM) (Life Technologies, Carlsbad, CA, http://www.lifetech.com) containing 10% heat-inactivated fetal bovine serum (FBS) (Life Technologies), penicillin (100 U/mL), and streptomycin (100 μg/mL) in 5% CO_2 in a humidified incubator at 37°C.

Cells and Cell Culture

The human osteosarcoma cell lines SaOS2, U2OS, MG63, HOS, MNNG/HOS, and 143B were purchased from the American Type Culture Collection (ATCC, Manassas, VA, http://www.atcc.org). The human osteosarcoma cell lines HuO9 and 143B-luc were previously established in our laboratory [29, 30], and SaOS2-luc cell line, a stable luciferase-expressing cell line, was newly established using a plasmid vector. We cultured SaOS2, SaOS-luc, and HuO9 cells in RPMI 1640 (Life Technologies). U2OS, MG63, HOS, MNNG/HOS, 143B, and 143B-luc cells were cultured in DMEM. All media were supplemented with 10% heat-inactivated FBS (Life Technologies), penicillin (100 U/mL), and streptomycin (100 μg/mL). The cells were maintained under 5% CO_2 in a humidified incubator at 37°C.

Cell Sorting and Flow Cytometry

Cell sorting by flow cytometry was performed on osteosarcoma cell lines and clinical samples using allophycocyanin (APC)-conjugated monoclonal mouse anti-human CD133/2 (293C3, Miltenyi Biotec, Auburn, CA, https://www.miltenyibiotec.com) and phycoerythrin (PE)-conjugated monoclonal mouse anti-human CD44 (eBioscience, San Diego, CA, http://www.ebioscience.com) antibodies. Isotype control mouse IgG2b-APC (Miltenyi Biotec) and mouse IgG2b-PE (eBioscience) served as a control. The samples were analyzed and sorted on a JSAN cell sorter (Bay Bioscience, Kobe, Japan, http://www.baybio.co.jp) and a BD FACS Aria II (BD Biosciences, Tokyo, Japan, http://www.bdbiosciences.com). Viability was assessed using propidium iodide (PI) to exclude dead cells. The results were analyzed using FlowJo software (Tree Star, San Carlos, CA, http://www.treestar.com).

Cell Proliferation and Cytotoxicity Assays

The cell proliferation rates and cell viability were used as indicators of the relative sensitivity of the cells to doxorubicin (DOX), cisplatin (CDDP), and methotrexate (MTX), and these measurements were determined using the TetraColor ONE Cell Proliferation Assay (Seikagaku, Tokyo, Japan, http://www.seikagaku.co.jp/) or Cell proliferation kit 8 (Dojindo, Kumamoto, Japan, http://www.dojindo.co.jp), according to the manufacturer's instructions. Cells growing in the logarithmic phase were seeded in 96-well plates (3×10^3 per well), allowed to attach overnight, and then treated with varying doses of doxorubicin (Sigma-Aldrich, St. Louis, MO, http://www.sigmaaldrich.com), CDDP (Enzo Life Sciences, Farmingdale, NY, http://www.enzolifesciences.com), or MTX (Sigma-Aldrich) for 72 hours in triplicate. The absorbance was measured at 450 nm with a reference wavelength at 620 nm using EnVision (Perkin-Elmer, Waltham, MA, http://www.perkinelmer.com). The relative number of viable cells was expressed as the percent of viable cells.

Sphere Formation

Freshly isolated $CD133^{high}$ and $CD133^{low}$ osteosarcoma SaOS2 cells were plated on ultra low-attachment 96-well plates (Corning, Corning, NY, http://www.corning.com) at a concentration of a single cell per well containing 100 μL of culture medium, which was confirmed visually. Wells containing either no cells or more than one cell were excluded for further analysis. The ratios of the wells containing spheres formed from single cells on day 10 were counted. The wells containing the cells that did not form spheres were excluded. The numbers of spheroids were counted 10 days after cell sorting. Serum-free DMEM/F12 (Life Technologies) supplemented with

20 ng/mL human recombinant epidermal growth factor (Sigma-Aldrich), 10 ng/mL human recombinant basic fibroblast growth factor (Life Technologies), 4 μg/mL insulin (Sigma-Aldrich), B27 (1:50; Life Technologies), 500 units/mL penicillin (Life Technologies) and 500 μg/mL streptomycin (Life Technologies) was used as the culture medium.

Invasion Assay

Invasion assays were performed using 24-well BD BioCoat Invasion Chambers with Matrigel (BD). A total of 1×10^5 cells were suspended in 500 μL DMEM or RPMI 1640 medium without FBS and added to the upper chamber. DMEM or RPMI 1640 medium with 10% FBS was added to the lower chamber. After incubation for 24 or 36 hours, the cells on the upper surface of the filter were completely removed by wiping with cotton swabs. The filters were fixed in methanol and stained with 1% toluidine blue in 1% sodium tetraborate (Sysmex, Kobe, Japan, http://www.sysmex.co.jp). The filters were mounted onto slides, and the cells on the lower surfaces were counted.

miRNA Profiling

miRNA expression profiling was performed using a miRNA microarray manufactured by Agilent Technologies (Santa Clara, CA, http://www.home.agilent.com) that contained 866 human miRNAs. Three independently extracted RNA samples obtained from $CD133^{high}$ and $CD133^{low}$ cells just after isolation were used for the array analyses. The labeling and hybridization of the total RNA samples were performed according to the manufacturer's protocol. The microarray results were extracted using the Agilent Feature Extraction software (v10.7.3.1) and analyzed using GeneSpring GX 11.0.2 software (Agilent Technologies).

Clinical Samples for Correlating Survival with the Expression of CD133, MiR-133a, and Targets of MiR-133a

The osteosarcoma tissue samples were obtained from diagnostic incisional biopsies of primary osteosarcoma sites before the start of neoadjuvant chemotherapy at the National Cancer Center Hospital of Japan between June 1997 and September 2010. We did not include patients older than 40 years or patients who had primary tumors located outside the extremities. Each fresh tumor sample was cut into two pieces; one piece was immediately cryopreserved in liquid nitrogen, and the other piece was fixed in formalin. The osteosarcoma diagnosis and the histological subtypes were determined by certified pathologists. Only osteosarcoma samples with the osteoblastic, chondroblastic, fibroblastic, or telangiectatic subtypes were included. The response to chemotherapy was classified as good if the tumor necrosis was 90% or greater. To correlate the survival studies with the expression of CD133 and the targets of miR-133a, 35 available cDNA samples from the cDNA library were used, and RNA from 48 available formalin-fixed paraffin-embedded (FFPE) samples were used for the correlation study with miR-133a expression. The patient clinical information is summarized in Supporting Information Table S1 and S2. All patients provided written, informed consent authorizing the collection and use of their samples for research purposes. The study protocol for obtaining clinical information and collecting samples was approved by the Institutional Review Board of the National Cancer Center of Japan.

RNA Isolation and Quantitative Real-Time Reverse Transcriptase Polymerase Chain Reaction of mRNAs and miRNAs

We purified total RNA from cells and tumor tissues using the miRNeasy Mini Kit (Qiagen, Valencia, CA, http://www.qiagen.com). For quantitative polymerase chain reaction (qPCR) of mRNAs, cDNA was synthesized using a High-Capacity cDNA Reverse Transcription Kit (Life Technologies). For each qPCR, equal amounts of cDNA were mixed with Platinum SYBR Green qPCR SuperMix (Life Technologies) and the specific primers (Supporting Information Table S3). We normalized gene expression levels to β-actin or GAPDH. For the qPCR of miRNAs, miRNA was converted to cDNA using the TaqMan MicroRNA Reverse Transcription Kit (Life Technologies). RNU6B small nuclear RNA was amplified as an internal control. qPCR was performed using each miRNA-specific probe included with the TaqMan MicroRNA Assay. The reactions were performed using a Real-Time PCR System 7300 with the SDS software (Life Technologies).

Transfection with Synthetic miRNAs, LNAs, and siRNAs

Synthetic hsa-miRs (Pre-miR-hsa-miR-1, 10b, 133a, and negative control (NC); Life Technologies; Supporting Information Table S4) and LNAs (LNA-1, 10b, 133a, and negative control; Exiqon, Vedbæk, Denmark, http://www.exiqon.com and Gene Design, Ibaraki, Japan, http://www.genedesign.co.jp, Supporting Information Table S5) were transfected into each cell line at 30 nM each (final concentration) using DharmaFECT one (Thermo Scientific, Yokohama, Japan, http://www.thermoscientific.jp). The synthetic siRNAs (Bonac Corporation, Kurume, Japan, http://www.bonac.com, Supporting Information Table S6) were transfected into cells at 100 nM each (final concentration) using DharmaFECT one (Thermo Scientific). After 24 hours of incubation, the cells were harvested and reseeded into a 6-well or 96-well plate.

Tumor Transplantation Experiments

The animal experiments in this study were performed in compliance with the guidelines of the Institute for Laboratory Animal Research at the National Cancer Center Research Institute. Athymic nude mice or NOD/SCID mice (CLEA Japan, Tokyo, Japan, http://www.clea-japan.com) were purchased at 4 weeks of age and given at least 1 week to adapt to their new environment prior to tumor transplantation. On day 0, the mice were anesthetized with 3% isoflurane, and the right leg was disinfected with 70% ethanol. The cells were aspirated into a 1 mL tuberculin syringe fitted with a 27-G needle. The needle was inserted through the cortex of the anterior tuberosity of the tibia with a rotating movement to avoid cortical fracture. Once the bone was traversed, the needle was inserted further to fracture the posterior cortex of the tibia. A 100 μL volume of solution containing SaOS2-luc cells (10^2, 10^3, 10^4, 10^5) or 143B-luc cells (1.5×10^6) was injected while slowly removing the needle.

Monitoring Tumor Growth, Lung Metastasis, and Toxicity with/Without LNA-Anti-MiR-133a

To evaluate LNA-133a administration to mice with spontaneous osteosarcoma lung metastases, individual mice were

injected with 10 mg/kg of LNA-133a or control LNA-NC (LNA-negative control) via the tail vain. LNAs were injected on days 4, 11, 18 postinoculation with the 143B-luc cells, followed by intraperitoneal injection of 3.5 mg/kg of CDDP on days 5, 12, and 19. Each experimental condition included 10 animals per group. The development of subsequent lung metastases was monitored once per week *in vivo* using bioluminescent imaging for 3 weeks. All data were analyzed using LivingImage software (version 2.50, Xenogen, Alameda, CA). On day 22, the primary tumors and lungs of five mice in each group were resected at necropsy for weight, bioluminescence, and histological analyses. A blood examination, weighing of the whole body, heart, liver, and skeletal muscle, and a histopathological examinations were performed for toxicity assessment. The remaining mice were observed for survival.

Comprehensive Collection and Identification of MiR-133a Target mRNAs

To identify comprehensive downstream targets of miR-133a, we performed cDNA microarray profiling using two experimental approaches. First, we collected candidate genes from the cDNA microarray analysis performed on total RNA collected from SaOS2 $CD133^{low}$ cells transfected with miR-133a or NC. Second, a cDNA microarray analysis was performed on total RNA collected using anti-Ago2 antibody immunoprecipitation (Ago2-IP) from $CD133^{low}$ cells transduced with miR-133a or NC. The genes that were identified in the former method as downregulated with a 1.5-fold decrease and the genes identified in the latter method as upregulated with a 2-fold increase were defined as candidates by reference to *in silico* databases using TargetScanHuman 6.0 (http://www.targetscan.org).

Luciferase Reporter Assays

Each fragment of the 3′ UTR of sphingomyelin synthase 2 (SGMS2) (nt 1,656–1,879 of NM_152621), ubiquitin-like modifier activating enzyme 2 (UBA2) (nt 2,527–2,654 of NM_005499), sorting nexin family member 30 (SNX30) (nt 6,659–7,611 of NM_001012944), and annexin A2 (ANXA2) (nt 1,056–1,634 of NM_001002857) were amplified and cloned into the XhoI and NotI sites of a psiCHECK-2 vector containing either the firefly or Renilla luciferase reporter gene (Promega, Tokyo, Japan, http://www.promega.com). We verified all PCR products that were cloned into the plasmid using DNA sequencing to ensure that they were free of mutations and in the correct cloning direction. The primer sequences are listed in Supporting Information Table S7. For the luciferase reporter assay, SaOS2 cells were cotransfected with 100 ng of luciferase constructs and 100 nM synthetic miR-133a molecules or control (nontargeting siRNA oligonucleotide, Qiagen). The firefly and Renilla luciferase activity levels were measured using the Dual-Luciferase Reporter Assay (Promega) 48 hours after transfection. The results are expressed as relative Renilla luciferase activity (Renilla luciferase/firefly luciferase).

Immunohistochemistry

To stain the miR-133a targets, we prepared slides from osteosarcoma xenograft tumors. Endogenous peroxidase was quenched with 1% H_2O_2 (30 minutes). The slides were heated for antigen retrieval in 10 mM sodium citrate (pH 6.0). Subsequently, we incubated the slides with monoclonal mouse anti-human SGMS2 (1:50 dilution, Abcam, Tokyo, Japan, http://www.abcam.co.jp), ANXA2 (1:250 dilution, Abcam), or isotype-matched control antibodies overnight at 4°C. Immunodetection was performed using ImmPRESS peroxidase polymer detection reagents (Vector Labs, Burlingame, CA, https://www.vectorlabs.com) and the Metal-Enhanced DAB Substrate Kit (Thermo Scientific) in accordance with the manufacturer's directions. The sections were counterstained with hematoxylin for contrast.

Statistical Analyses

All statistical analyses were performed using SPSS Statistics Version 21 software (IBM SPSS, Tokyo, Japan, https://www.ibm.com). Student's t test or one-way ANOVA, corrected for multiple comparisons as appropriate, was used to determine the significance of any differences between experimental groups. The differences in CD133, miR-133a, and the miR-133a targets expression among different clinicopathological data were analyzed using the chi-squared (χ^2) test or ANOVA. We carried out receiver-operating characteristic curve analysis using the SPSS software, and the optimal cutoff points for the expression levels of CD133, miR-133a, and the target genes of miR-133a were determined by the Youden index, that is, J = max (sensitivity + specificity − one) [31]. The Kaplan-Meier method and the log-rank test were used to compare the survival of patients. We defined the survival period as the time from diagnosis until death, whereas living patients were censored at the time of their last follow-up. For all the analyses, we considered a p value of .05 or less to be significant.

Results

Osteosarcoma $CD133^{high}$ Cell Populations Are Enriched with Highly Malignant Cells with the Multiple Phenotypes

Based on the emerging evidence that tumors contain the heterogeneous cell populations, we tried to isolate the small population of highly malignant cells in osteosarcoma. In order to evaluate the phenotypes of the cell population, we screened human osteosarcoma cell lines (SaOS2, U2OS, HOS, MG-63, HuO9, MNNG/HOS, and 143B) for the markers expressed on the highly malignant cell populations within the tumors [4, 7, 32]. As a result, we confirmed that CD133, a human structural homolog of mouse prominin-1, was expressed in a small proportion of cells ranging from 0.04% to 8.47% (Fig. 1A; Supporting Information Fig. S1A), which was consistent with the previous reports [18, 19]. Several examinations were performed to confirm the phenotypes of the SaOS2 $CD133^{high}$ and $CD133^{low}$ populations. Freshly isolated $CD133^{high}$ and $CD133^{low}$ osteosarcoma SaOS2 cells were plated at a concentration of a single cell and cultured immediately in a serum-free, growth factor-supplemented, anchorage-independent environment. Within 2 weeks of culture, we observed more osteosarcoma spheres from the $CD133^{high}$ cells than from the $CD133^{low}$ cells (Fig. 1B, 1C). The cell proliferation rate was slightly lower in $CD133^{high}$ cell population than in $CD133^{low}$ cell population (Supporting Information Fig. S1D). To assess the difference of drug resistance, both populations were observed after exposure to doxorubicin (DOX), cisplatin (CDDP), or methotrexate (MTX), which are the standard

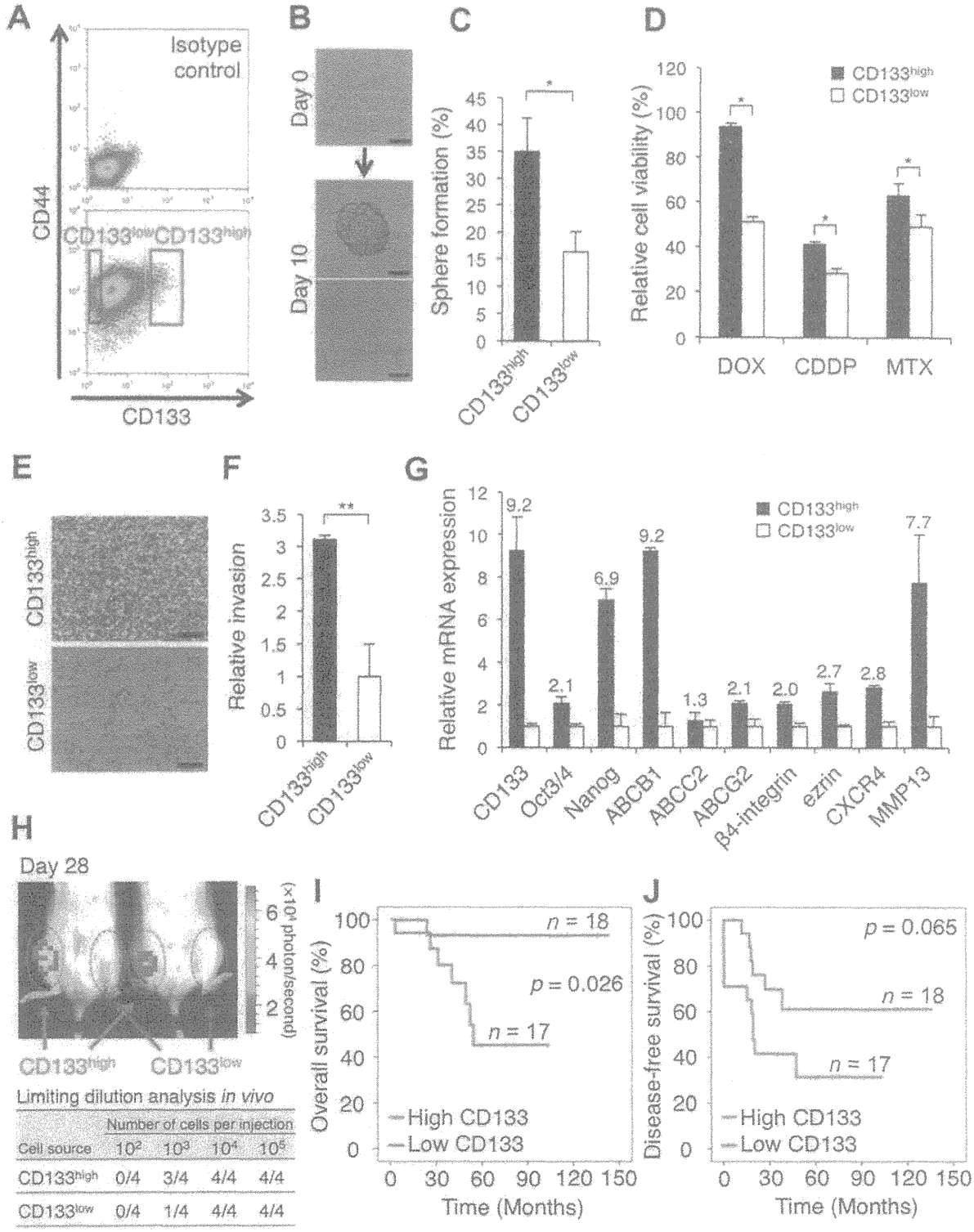

Figure 1. The phenotypic differences and clinical relevance based on the expression of CD133 in osteosarcoma cells. **(A):** The frequency of CD133^{high} cell populations in SaOS2 osteosarcoma cell lines based on fluorescence-activated cell sorting analysis. See also Supporting Information Figure S1A. **(B, C):** Sphere-formation assays using freshly isolated CD133^{high} and CD133^{low} SaOS2 cells. The images were captured on day 10 (B), and the ratios of the wells containing spheres (middle) formed from single cells (top) were counted (C). The wells containing the cells that did not form spheres (bottom) were excluded. Scale bar = 50 μm. Data are presented as mean ± SD ($n = 4$ per group). *, $p < .05$; Student's t test. **(D):** Drug sensitivity of CD133^{high} and CD133^{low} SaOS2 cells. Cell viability after DOX (0.18 μM), CDDP (2.5 μM), or MTX (0.08 μM) treatment was analyzed. Data are presented as mean ± SD ($n = 3$ per group). *, $p < .05$; Student's t test. **(E, F):** Invasion assays in CD133^{high} and CD133^{low} SaOS2 cell populations ($n = 3$ per group). The number of invaded cell were photographed (E) and counted (F). Data are presented as mean ± SD ($n = 3$ per group). **, $p < .01$; Student's t test. Scale bar = 200 μm. **(G):** Quantitative polymerase chain reaction analysis of stem cell-associated, multiple drug-resistant transporters, and metastasis-associated genes of CD133^{high} and CD133^{low} SaOS2 cell populations. β-Actin was uses as an internal control. Data are presented as mean ± SD ($n = 3$ per group). **(H):** Limiting dilution analysis of CD133^{high} (red circles) and CD133^{low} (green circles) SaOS2-luc cell populations *in vivo*. Both cell populations were injected orthotopically into mice ($n = 4$ per group). The upper figure represents the tumor formation in mice from 1×10^3 cells of CD133^{high} cells. The lower table shows the number of mice that developed tumors from various numbers of CD133^{high} or CD133^{low} cells. The tumor growth from CD133^{high} cells was observed in 0/4 mice at 10^2 cells, 3/4 mice at 10^3 cells, 4/4 mice at 10^4 cells, and 4/4 mice at 10^5 cells, while those from CD133^{low} cells was observed in 0/4 mice at 10^2 cells, 1/4 mice at 10^3 cells, 4/4 mice at 10^4 cells, and 4/4 mice at 10^5 cells. **(I, J):** The Kaplan-Meier curves for overall survival (I; $p = .026$; log-rank test) and disease-free survival (J; $p = .065$, log-rank test) based on the level of CD133 expression in the biopsy specimens from 35 osteosarcoma patients. See also Supporting Information Figure S2A and Table S1. *Abbreviations: CDDP, cisplatin; DOX, doxorubicin; MTX, methotrexate.*

chemotherapeutic agents that are used against osteosarcoma. The $CD133^{high}$ cells were more resistant to these chemotherapeutics than $CD133^{low}$ cells (Fig. 1D). In addition, $CD133^{high}$ cells showed a higher invasive ability than $CD133^{low}$ cells (Fig. 1E, 1F). Performing qRT-PCR reactions on mRNA from freshly isolated $CD133^{high}$ and $CD133^{low}$ cells revealed that $CD133^{high}$ SaOS2 cells expressed higher levels of *Oct3/4* and *Nanog*, which are essential transcription factors that play critical roles in the self-renewal and pluripotency of embryonic stem cells (Fig. 1G) [15–17]. Meanwhile, the expression levels of the genes that are essential for differentiation, such as *Runx2*, *Osterix*, and *Sox9* [33–36], were lower in $CD133^{high}$ than in $CD133^{low}$ cells (Supporting Information Fig. S1C). In addition, the multidrug resistance transporter genes *ABCB1*, *ABCC2*, and *ABCG2* and the metastasis-associated genes *β4-integrin*, *ezrin*, *MMP-13*, and *CXCR4* [30, 37] were upregulated in $CD133^{high}$ cells relative to $CD133^{low}$ cells (Fig. 1G). Importantly, the $CD133^{high}$ SaOS2 cells showed stronger tumorigenicity *in vivo* than the $CD133^{low}$ SaOS2 cells (Fig. 1H). We identified tumor initiation on the right legs of three in four mice transplanted with 1×10^3 $CD133^{high}$ cells but only one in four mice formed tumor with 1×10^3 $CD133^{low}$ cells on the left legs. To evaluate the clinical importance of CD133 expression, cell lines established from fresh human osteosarcoma biopsies were analyzed by flow cytometry, and these cell lines contained a low proportion (< 10%) of $CD133^{high}$ cells (Supporting Information Fig. S1B). Furthermore, a clinical study of 35 osteosarcoma patients revealed that high expression levels of CD133 mRNA were associated with significantly worse survival rates among osteosarcoma patients (Fig. 1I, 1J; Supporting Information Figure S2A). In this study, all biopsy samples from patients who developed lung metastasis at first diagnosis represented high expression level of CD133 ($p = .045$; Supporting Information Table S1), suggesting that the expression of CD133 closely correlate with osteosarcoma metastasis. Collectively, the osteosarcoma $CD133^{high}$ cell population possessed highly malignant phenotypes, and the expression of CD133 revealed a prognostic value of osteosarcoma patients.

MiR-133a Functions as a Key Regulator of Malignant Phenotypes in Osteosarcoma

Following the confirmation of the malignant phenotypes in the osteosarcoma $CD133^{high}$ population, we further characterized the molecular mechanisms underlying these phenotypes. We focused on miRNAs because of their ability to simultaneously regulate multiple pathways responsible for the malignant phenotypes by targeting multiple genes. miRNAs are small, regulatory RNA molecules that modulate the post-transcriptional expression of their target genes and play important roles in a variety of physiological and pathological processes, including tumor biology [23, 25, 38]. miRNA expression profiling has become a useful diagnostic and prognostic tool, and many studies have indicated that miRNAs act as either oncogenes or tumor suppressors [38]. In our miRNA microarray analysis of isolated $CD133^{high}$ and $CD133^{low}$ cells using 866 sequence-validated human miRNAs, we identified 20 miRNAs that were upregulated in $CD133^{high}$ cells and additional qRT-PCR analysis demonstrated that the expression levels of miR-1 and miR-10b, together with miR-133a, which represents the "miR-1 cluster" transcribed from adjacent miR-1 genes, were consistent with the microarray data (Fig. 2A; Supporting Information Fig. S3A, Table S8). Indeed, miR-1 and miR-133a are physically linked, and both the miR-1-1/miR-133a-2 (chromosome 20q13.33) as well as miR-1–2/miR-133a-1 clusters (chromosome 18q11.2) are present. miR-10b is embedded in the *HOX* gene cluster and maps between the *HOXD3* and *HOXD4* genes on chromosome 2q31. Since miR-10a and miR-133b would presumably be functionally redundant to miR-10b and miR-133b, respectively, we also confirmed that miR-133b, but not miR-10a, was upregulated in $CD133^{high}$ cell population (Supporting Information Fig. S3B).

To determine whether these miRNAs could regulate the malignant phenotypes of osteosarcoma, we manipulated the expression levels of miR-1, 10b, and 133a in $CD133^{low}$ cells (Supporting Information Fig. S4A). These miRNAs, especially miR-133a, enhanced the invasiveness of $CD133^{low}$ cells compared with control oligos (Fig. 2B, 2C). Interestingly, the combined transfection of all of these miRNAs enhanced the invasiveness of $CD133^{low}$ cells to the greatest extent (Fig. 2C). However, the transfection of miR-133a did not increase the mRNA level of CD133 (Supporting Information Fig. S4B), suggesting that miR-133a does not affect the expression of the molecules upstream of CD133. These results indicated that miR-133a simultaneously regulate several molecular pathways that are associated with cell invasion of the malignant cell population within osteosarcoma. In our experiment using fresh clinical samples, miR-133a expression was also high in the $CD133^{high}$ fraction of osteosarcoma biopsies (Fig. 2D). Surprisingly, a clinical study based on qRT-PCR using clinical FFPE samples revealed that the high expression of miR-133a closely correlated with a poor prognosis of osteosarcoma patients (log-rank test, $p = .032$ for overall survival, $p = .081$ for disease-free survival; Fig. 2E, 2F; Supporting Information Fig. S2B, Table S2).

Silencing of MiR-133a Inhibits the Cell Invasion of $CD133^{high}$ Osteosarcoma Cell Population

To evaluate whether silencing of miR-133a show the therapeutic effect on osteosarcoma cells, we manipulated the expression of miR-133a by introducing LNAs. LNAs are a class of nucleic acid analogs that possess a very high affinity and excellent specificity toward complementary DNA and RNA, and LNA oligonucleotides have been applied as antisense molecules both *in vitro* and *in vivo* [39–41]. The SaOS2 $CD133^{high}$ cell population was isolated by cell sorting and was then transfected with LNA-antimiR-133a (LNA-133a) and LNA-NC. As a control, the isolated SaOS2 $CD133^{low}$ cell population was also transfected with LNA-NC. Prior to functional assay, we confirmed the efficacy of LNA-133a using both qRT-PCR analysis and a sensor vector which allowed us to measure the suppressive effect of LNA by luciferase assay (Supporting Information Fig. S5A–S5D). We observed that the LNA-133a-treated SaOS2 $CD133^{high}$ cells demonstrated decreased invasiveness relative to LNA-NC-treated $CD133^{high}$ cells, whereas there was no significant difference of cell proliferation between the two populations (Fig. 2G, 2H; Supporting Information Fig. S5E). These observations suggest that silencing of miR-133a in $CD133^{high}$ cells could reduce the cell invasion of the malignant cell population within osteosarcoma tissue.

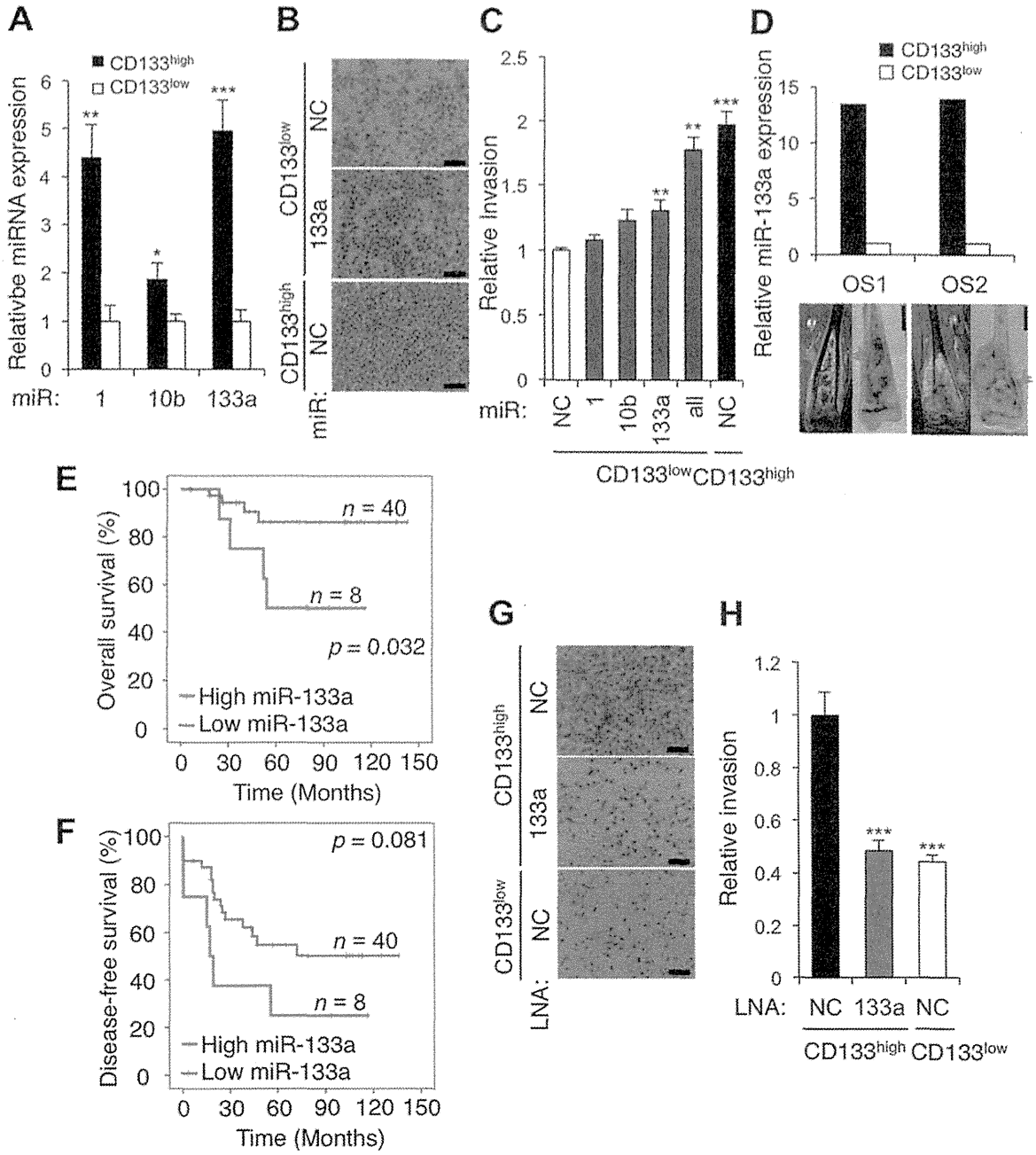

Figure 2. MiR-133a regulates cell invasion of tumor-initiating cell population within osteosarcoma and represents prognostic value. **(A):** The upregulated expression levels of miR-1, 10b, and 133a in CD133^{high} cell population. Data are presented as mean ± SD ($n = 3$ per group). *, $p < .05$; **, $p < .01$; ***, $p < .001$; Student's t test. **(B, C):** Invasion assays in purified CD133^{low} SaOS2 cells transfected with miR-1, 10b, and 133a oligos. CD133^{low} SaOS2 cell populations were transfected with miR-1, 10b, 133a, or NC mimics at a final concentration of 30 nM. At the time periods of 24 hours post-transfection, cells were seeded and cultured on the invasion chamber for 36 hours. The number of invaded cell were photographed (B) and counted (C). Scale bar = 200 μm. Data are presented as mean ± SD ($n = 3$ per group). **, $p < .01$; ***, $p < .001$, calculated with one-way ANOVA with Bonferroni's multiple comparison when compared with the CD133^{low} cell population treated with miR-NC. **(D):** The expression level of miR-133a in CD133^{high} and CD133^{low} populations of freshly resected patient biopsies. **(E, F):** The Kaplan-Meier curves for overall survival (E) and disease-free survival (F) based on the levels of miR-133a expression in 48 formalin-fixed paraffin-embedded tissues from osteosarcoma biopsy specimens, as determined using quantitative reverse transcriptase polymerase chain reaction. The overall survival rate ($p = .032$; log-rank test) and disease-free survival rate ($p = .081$; log-rank test) for osteosarcoma patients with high miR-133a expression (red line) were compared with those for patients with low miR-133a expression (green line). See also Supporting Information Figure S2B and Table S2. **(G, H):** Invasion assays in LNA-133a-treated SaOS2 CD133^{high} populations. CD133^{high} and CD133^{low} SaOS2 cell populations were isolated and transfected with LNA-133a or LNA-NC to reduce the expression of miR-133a in the CD133^{high} cell population. As a control, CD133^{low} cell populations were transfected with LNA-NC. At the time periods of 24 hours post-transfection, cells were seeded and cultured on the invasion chamber for 36 hours. The number of invaded cell were photographed (G) and counted (H). Scale bar = 200 μm. Data are presented as mean ± SD ($n = 3$ per group). ***, $p < .001$, calculated with one-way ANOVA with Bonferroni's multiple comparison when compared with the CD133^{high} cell populations treated with LNA-NC. Abbreviations: LNA, locked nucleic acid; NC, negative control.

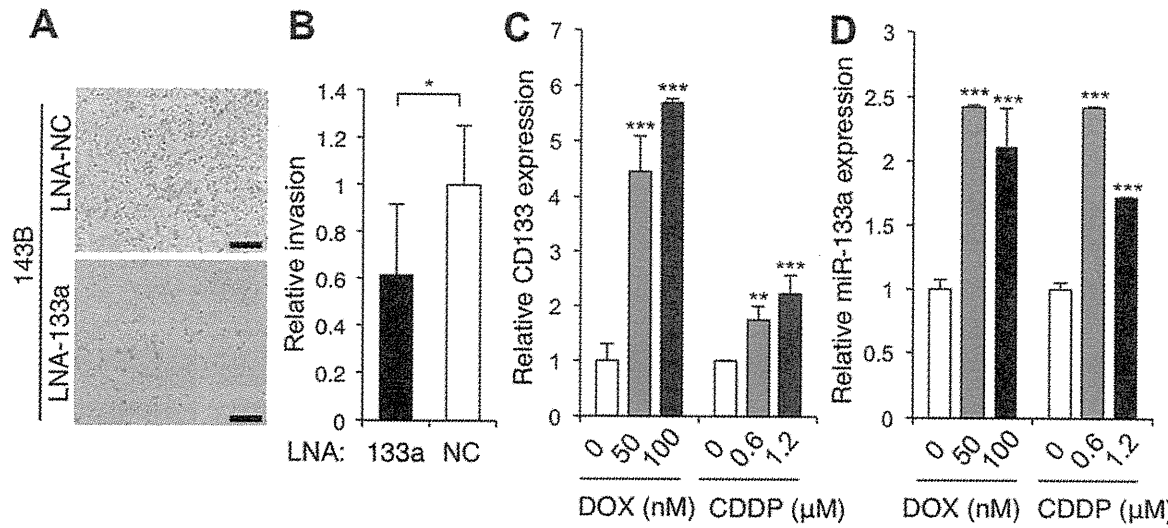

Figure 3. Chemotherapy induces the expression of miR-133a in highly malignant osteosarcoma 143B cells. **(A, B):** Invasion assay in highly metastatic osteosarcoma 143B cells treated with LNA-133a and NC. At the time periods of 24 hours post-transfection, cells were seeded and cultured on the invasion chamber for 24 hours. The number of invaded cell were photographed (A) and counted (B). Scale bar = 200 μm. Data are presented as mean ± SD ($n = 3$ per group). *, $p < .05$; Student's t test. **(C):** The induced expression of CD133 in 143B cells in the presence of chemotherapeutics (DOX and CDDP, 48 hours). Data are presented as mean ± SD ($n = 3$ per group). **, $p < .01$; ***, $p < .001$, calculated with one-way ANOVA with Bonferroni's multiple comparison when compared with untreated cells. **(D):** The induced expression of miR-133a in 143B cells in the presence of chemotherapeutics (DOX and CDDP, 48 hours). Data are presented as mean ± SD ($n = 3$ per group). ***, $p < .001$, calculated with one-way ANOVA with Bonferroni's multiple comparison when compared with untreated cells. Abbreviations: CDDP, cisplatin; DOX, doxorubicin; LNA, locked nucleic acid; NC, negative control.

The Expression Levels of MiR-133a in Osteosarcoma Cells Are Enhanced by Chemotherapy

Next, we validated the efficacy of LNA-133a on highly malignant metastatic osteosarcoma 143B cells, since SaOS2 cells represent low metastatic ability *in vivo* [42, 43]. Meanwhile, we needed to evaluate the efficacy of LNA on "bulk" 143B cells, assuming clinical situations. As a result, LNA-133a reduced the invasiveness of 143B cells (Fig. 3A, 3B) but did not influence cell proliferation (Supporting Information Fig. 5F). Since recent study has indicated a novel mechanism of chemotherapy-induced tumor progression via expansion of TIC population [44], the expression levels of CD133 and the related miR-133a within cells treated with or without chemotherapeutics were analyzed. As a result, we observed that the expression levels of miR-133a, together with CD133, were enhanced by chemotherapy. qRT-PCR analysis revealed that DOX-treated or CDDP-treated (2 days) 143B cells expressed higher levels of CD133 and miR-133a compared with untreated 143B cells (Fig. 3C, 3D). Therefore, silencing of miR-133a before or during chemotherapy may prevent the increased expression of miR-133a, which enhanced the malignant phenotypes and was induced by chemotherapeutics.

Therapeutic Administration of LNA-133a with Chemotherapy Inhibits Spontaneous Lung Metastasis and Prolongs the Survival of Osteosarcoma-Bearing Mice

To extend our *in vitro* findings and to determine whether silencing of miR-133a could be an effective therapeutic option for osteosarcomas, we next examined the effect of LNA-133a on a spontaneous lung metastasis model of osteosarcoma. Experimentally, 1.5×10^6 143B cells transfected with the firefly luciferase gene (143B-luc) were implanted orthotopically into the right proximal tibia of athymic nude mice. The implanted tumor growth and the presence of distant metastases were analyzed weekly for luciferase bioluminescence using an *in vivo* imaging system. We used a new treatment protocol (Fig. 4A) with the intravenous (i.v.) administration of LNA-133a (10 mg/kg) 24 hours before intraperitoneal (i.p.) injection of CDDP (3.5 mg/kg) to prevent the induction of malignant phenotypes by chemotherapy, which were indicated in the *in vitro* experiments. Prior to conducting these animal studies, we confirmed that miR-133a levels were reduced in osteosarcoma tissues from LNA-133a-treated mice compared with control mice (Supporting Information Fig. S6A, S6B). To assess the efficacy of our protocol, the results were compared with the results obtained for the following four control groups ($n = 10$ per group): the control saline followed by control saline group, the LNA-NC followed by control saline group, the LNA-133a followed by control saline group, and the LNA-NC followed by CDDP group. After implantation of the 143B-luc cells, five mice within each one cage were sacrificed at 3 weeks after evaluating lung metastasis by *in vivo* imaging and validated for lung metastasis formation by additional *in vivo* imaging and histological examination of the lung, whereas the other five mice in the other cage were evaluated for survival periods. The results demonstrated that the tumor expression levels of miR-133a were decreased in the presence of LNA-133a (Fig. 4B). Although tumor growth at the primary site was significantly reduced in CDDP-treated group, we identified no significant difference between LNA-133a-CDDP-treated mice and LNA-NC-CDDP-treated mice (Fig. 4C, 4D). We observed lung metastases on day 22 in nine (90%) saline-saline-treated mice, eight (80%) LNA-NC-saline-treated mice, seven (70%) LNA-133a-saline-treated mice, eight (80%) LNA-NC-CDDP-treated mice, and three (30%) LNA-133a-CDDP-

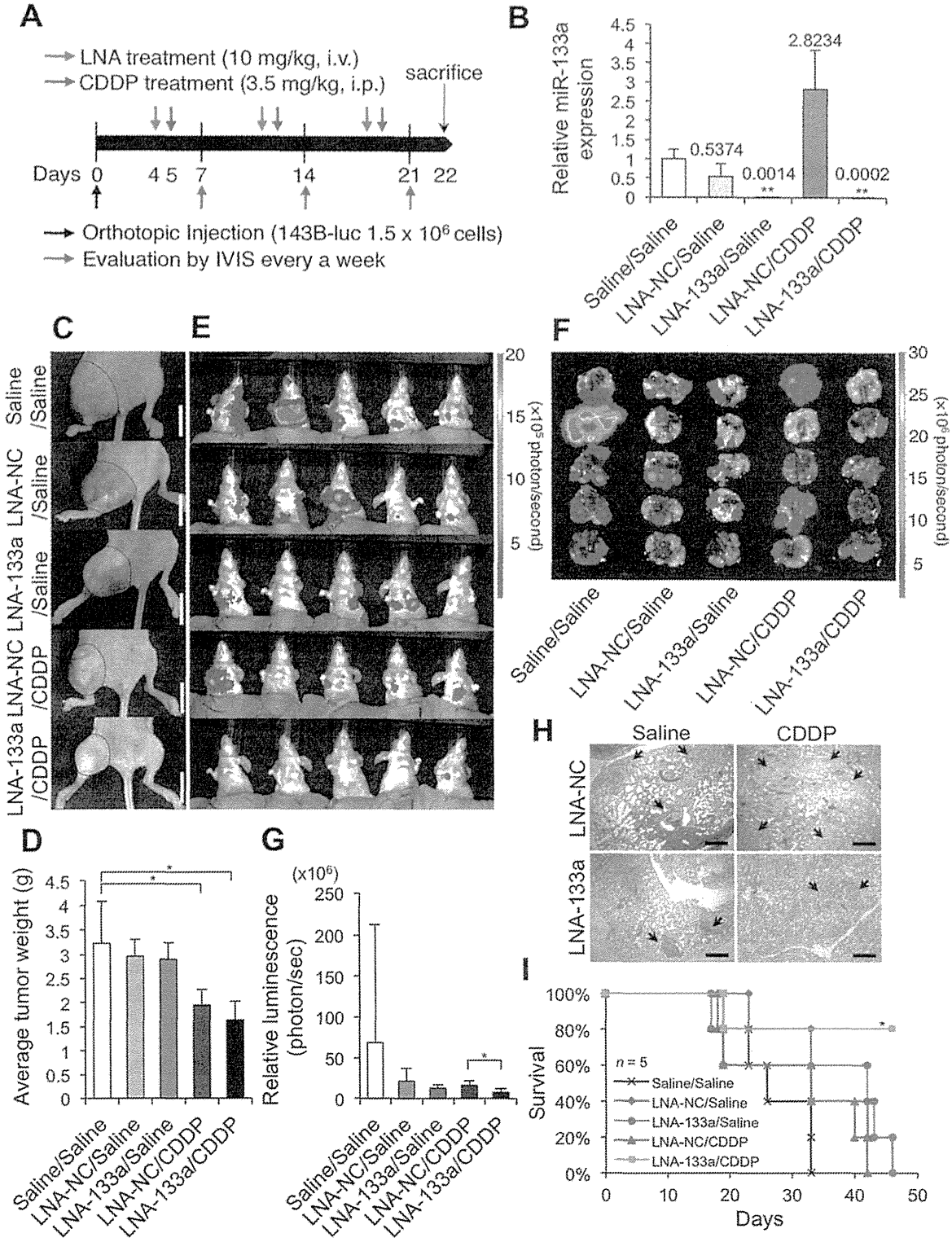

Figure 4. Therapeutic administration of LNA-133a with systemic chemotherapy inhibits osteosarcoma progression *in vivo*. **(A):** A schematic representation of the LNA-133a (red arrow) and CDDP (blue arrow) administration schedule for 143B-luc-bearing mice. **(B):** The expression levels of miR-133a in osteosarcoma tissues ($n = 5$ per group) analyzed by quantitative reverse transcriptase polymerase chain reaction. The tumors were obtained during autopsy after completion of treatment on day 22. Data are presented as mean ± SD ($n = 5$ per group). **, $p < .01$, as compared to control saline-treated group; Student's *t* test. **(C, D):** Tumors at the primary site of each treatment group measured on day 22. The macroscopic appearances of 143B-luc tumors in each group of mice on day 22 are shown (C). The tumor masses outlined by a dotted line. Scale bar = 10 mm. The 143B-luc tumors from each group of mice were weighed on day 22 (D). Data are presented as mean ± SD ($n = 5$ per group). *, $p < .05$, as compared to control saline-treated group; Student's *t* test. **(E–G):** The lung metastases of each treatment group measured on day 22 using an IVIS. The representative luminescence of the chest regions in each group of mice was determined (E). For each mouse that was sacrificed to validate the lung metastases, each lung was re-evaluated using IVIS (F). The representative average luminescence of the chest region in each group of mice ($n = 10$) was compared among the treatment groups (G). Data are presented as mean ± SD ($n = 5$ per group). *, $p < .05$, as compared with LNA-NC/CDDP and LNA-133a/CDDP group; Student's *t* test. **(H):** Lung metastases validated by H&E staining. Black arrow represents metastatic foci in the lung. Scale bars = 500 μm. **(I):** Survival curves for each group of mice by Kaplan-Meier analysis. Log-rank test was performed between LNA-NC/CDDP group (blue line) and LNA-133a/CDDP group (red line) (*, $p = .026$). Abbreviations: CDDP, cisplatin; IVIS, *in vivo* imaging system; LNA, locked nucleic acid; NC, negative control.

treated mice ($n = 10$; Fig. 4E, 4F). We observed the decreased signal intensity in the chest regions of LNA-133a-CDDP-treated mice compared to those of LNA-NC-CDDP-treated mice (Fig. 4G). Both the number and size of lung metastases were validated by histopathological examination (Fig. 4H). We found low cell concentration in lung metastatic foci of CDDP-treated groups, indicating therapeutic effect of chemotherapy, and identified smallest number of osteosarcoma metastatic foci in the lung of LNA-133a-CDDP-treated mice. Furthermore, LNA-133a-CDDP-treated mice showed longest survival periods among the five groups in Kaplan-Meier analysis (log-rank test, $p = .026$; Fig. 4I). Despite the conserved sequence of mature hsa-miR-133a and mmu-miR-133a (Supporting Information Fig. S7A), all mice exhibited minimal toxic effects on various tissues, including the heart, liver, skeletal muscle, and blood test, during the observation period (Supporting Information Fig. S7B–S7H, S8A–S8I). Thus, systemic administration of LNA-133a was effective for the suppression of lung metastases in a xenograft model of a highly metastatic osteosarcoma in the presence of CDDP.

Multiple Target Genes of MiR-133a Function as Regulators of Cell Invasion and Closely Correlate with Clinical Behavior of Osteosarcoma

We demonstrated that miR-133a regulated the malignancy of $CD133^{high}$ osteosarcoma cell population and that silencing of miR-133a expression with chemotherapeutics inhibited the osteosarcoma metastasis *in vivo*. Next, to understand the molecular mechanism regulated by miR-133a in the tumor-initiating population, we performed mRNA expression profiling using two different microarray analyses together with *in silico* predictions (Supporting Information Fig. S9A). We detected 1,812 genes that were downregulated by at least 1.2-fold in the first microarray analysis, which was performed from total RNA collected from SaOS2 $CD133^{low}$ cells transduced with miR-133a or NC. Furthermore, 4,976 genes were upregulated by at least 2-fold in the second microarray analysis of mRNA expression using RNA collected using anti-Argonaute 2 antibody immunoprecipitation (Ago2 IP) in $CD133^{low}$ cells transduced with miR-133a or NC. Subsequently, 226 genes were collected using both methods, and 20 genes were identified in TargetScanHuman 6.0, a publicly available *in silico* database (Fig. 5A). Overall, 10 putative miR-133a target genes were selected from these combined data, and we reduced the expression of these molecules using an siRNA-induced gene knockdown system to investigate whether these candidates are functionally important targets of miR-133a in osteosarcoma cells. As a result, the knockdown of four genes (*SGMS2*, *UBA2*, *SNX30*, and *ANXA2*) enhanced the invasiveness of $CD133^{low}$ SaOS2 cells (Fig. 5B). To validate whether these molecules are regulated by miR-133a, we cloned the 3′ UTR fragment (Fig. 5C) containing the putative miR-133a binding sites downstream of a luciferase coding sequence and performed cotransfection of the luciferase reporter and miR-133a oligos in SaOS2 cells. Luciferase activity levels were reduced by approximately 36%–55% in the cells cotransfected with miR-133a compared with the cells cotransfected with the NC oligos (Fig. 5D). Consequently, *SGMS2*, *UBA2*, *SNX30*, and *ANXA2* functioned as direct targets of miR-133a. Indeed, these molecules have been suggested to have antitumor function in the other types of tumors [45–47]. Among them, *ANXA2* is downregulated in osteosarcoma metastases compared to primary site [48]. The expression levels of these targets were decreased in $CD133^{high}$ cells (Supporting Information Fig. S9B) and reduced via miR-133a upregulation in $CD133^{low}$ cells (Supporting Information Fig. S9C). The increased expression levels of the targets after silencing of miR-133a were confirmed by immunohistochemistry of LNA-treated tumors and qRT-PCR (Fig. 5E, 5F; Supporting Information Fig. S9D). Taken together, LNA-133a was found to inhibit cell invasion of the malignant cell population of osteosarcoma through multiple molecular pathways. Finally, we observed a strikingly close correlation between these mRNA expression levels of the miR-133a targets and osteosarcoma patient prognosis (Fig. 6A–6D). Patients with higher expression levels of these targets significantly survived longer than those with lower expression levels. These results would support the importance of regulating the expression of miR-133a during current osteosarcoma treatment, providing insight into the development of more effective therapies against osteosarcoma.

Discussion

Cancer researchers today are confronted with how to overcome the natural resistance and the acquired resistance of cancer cells within tissue, despite the many cancer treatment options. The CSC or TIC hypothesis has been an attractive model to account for the functional heterogeneity that is commonly observed in solid tumors [7]. To characterize and eliminate the malignant cells in cancers that follow this model, it has been necessary to focus on the small subpopulations of tumorigenic cells [49]. Tremendous efforts and evidence have accumulated to identify these subpopulations [13–18, 20, 21]. However, these markers are generally difficult to be targeted because of their distribution on the normal stem cells. For example, targeting CD133 seems unsafe because this cell-surface protein is primarily expressed in stem and progenitor cells [50] such as the embryonic epithelium [51], brain stem cells [52], and hematopoietic stem cells [32, 53]. Therefore, the molecular mechanisms underlying the malignant phenotypes must be elucidated to avoid toxicities, which have not been fully accomplished. On the basis of our results, we propose novel therapeutic strategies, beyond the use of traditional antiproliferative agents, for suppression of the highly malignant cell population within osteosarcoma using RNAi therapeutics, which is expected to be the "next-generation" anticancer strategy. Subsequently, we present four novel discoveries that were identified in a preclinical trial of novel therapeutic strategies against osteosarcoma.

First, we identified human miR-133a as a key regulator of the malignant tumor-initiating phenotypes of osteosarcoma. The other miRNAs that might regulate these phenotypes included miR-1 and miR-10b. The human miRNA hsa-miR-10b is also positively associated with high-grade malignancies, including breast cancer [54, 55], pancreatic adenocarcinomas [56], and glioblastomas [57]. However, the importance of miR-10b in sarcoma development has not been previously reported. In our experiment, miR-10b regulated, less than miR-133a, the cell invasion of osteosarcoma. The human miRNAs hsa-miR-1 and hsa-miR-133a are located on the same chromosomal region in a so-called cluster. We found that miR-

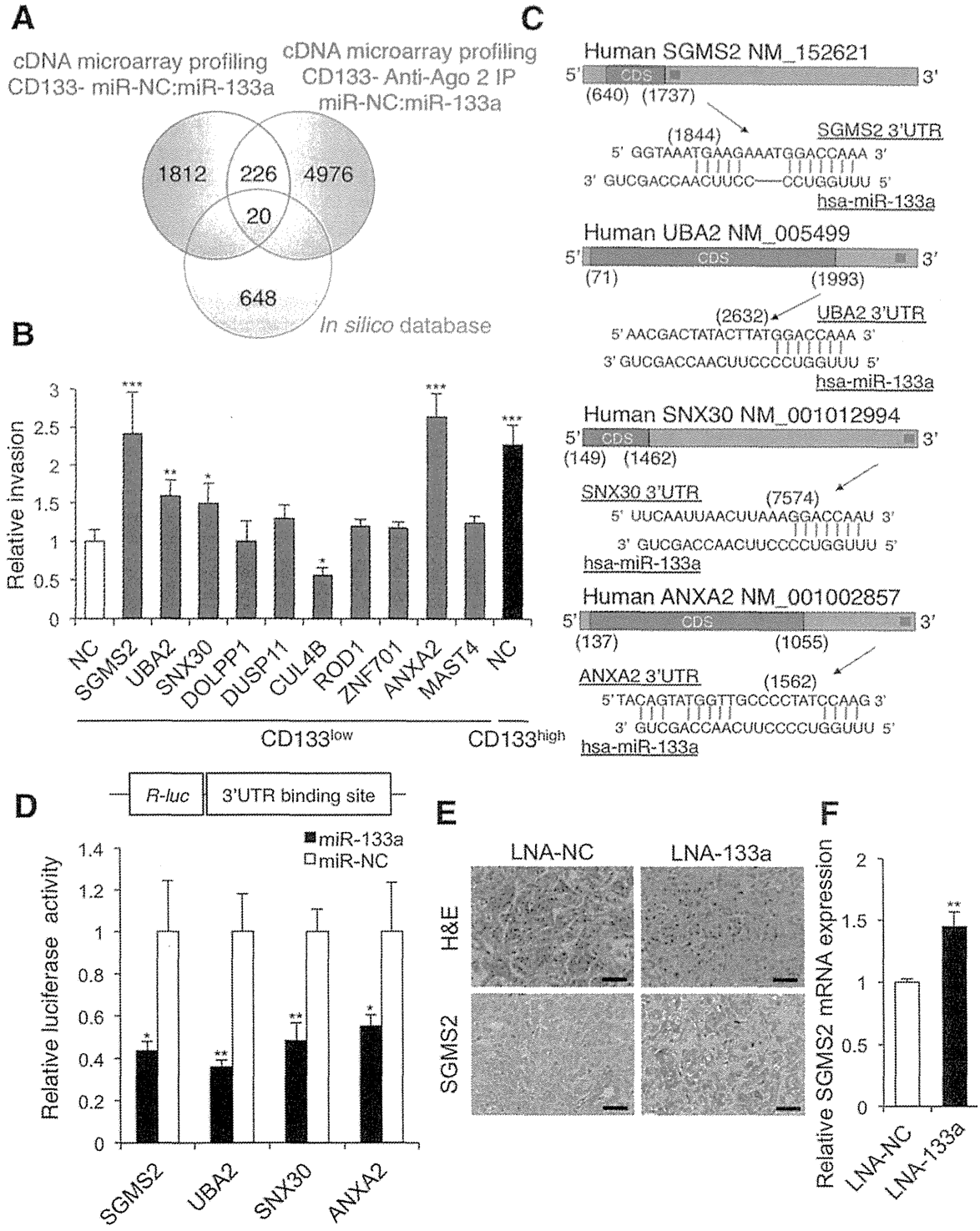

Figure 5. The direct target genes of miR-133a regulate malignant phenotypes of osteosarcoma. **(A):** A Venn diagram of the candidate target mRNAs of miR-133a based on the cDNA microarrays and *in silico* database. **(B):** Invasion assays performed using SaOS2 cells 24 hours post-transfection of the 10 siRNAs. $CD133^{high}$ and $CD133^{low}$ SaOS2 cell populations were isolated using flow cytometry and transfected with 10 siRNAs against the identified genes in **(A)**. Data are presented as mean ± SD ($n = 3$ per group). *, $p < .05$; **, $p < .01$; ***, $p < .001$, calculated with one-way ANOVA with Bonferroni's multiple comparison when compared with the $CD133^{low}$ cells transfected with nontargeting siRNA. **(C):** Schematics of the miR-133a binding site within the 3′ UTR of the target mRNAs. **(D):** Luciferase activities measured by cotransfecting miR-133a oligos and the luciferase reporters. Data are presented as mean ± SD ($n = 3$ per group). *, $p < .05$; **, $p < .01$; Student's *t* test. **(E, F):** Representative SGMS2 immunohistochemistry images of 143B-luc tumor sections (E) and the relative SGMS2 expression of 143B-luc tumor sections performed by quantitative reverse transcriptase polymerase chain reaction analysis (F). Scale bars = 50 μm. Data are presented as mean ± SD ($n = 3$ per group). **, $p < .01$; Student's *t* test. Abbreviations: ANXA2, annexin A2; IP, immunoprecipitation; LNA, locked nucleic acid; NC, negative control; SGMS2, sphingomyelin synthase 2; SNX30, sorting nexin family member 30; UTR, untranslated region; UBA2, ubiquitin-like modifier activating enzyme 2.

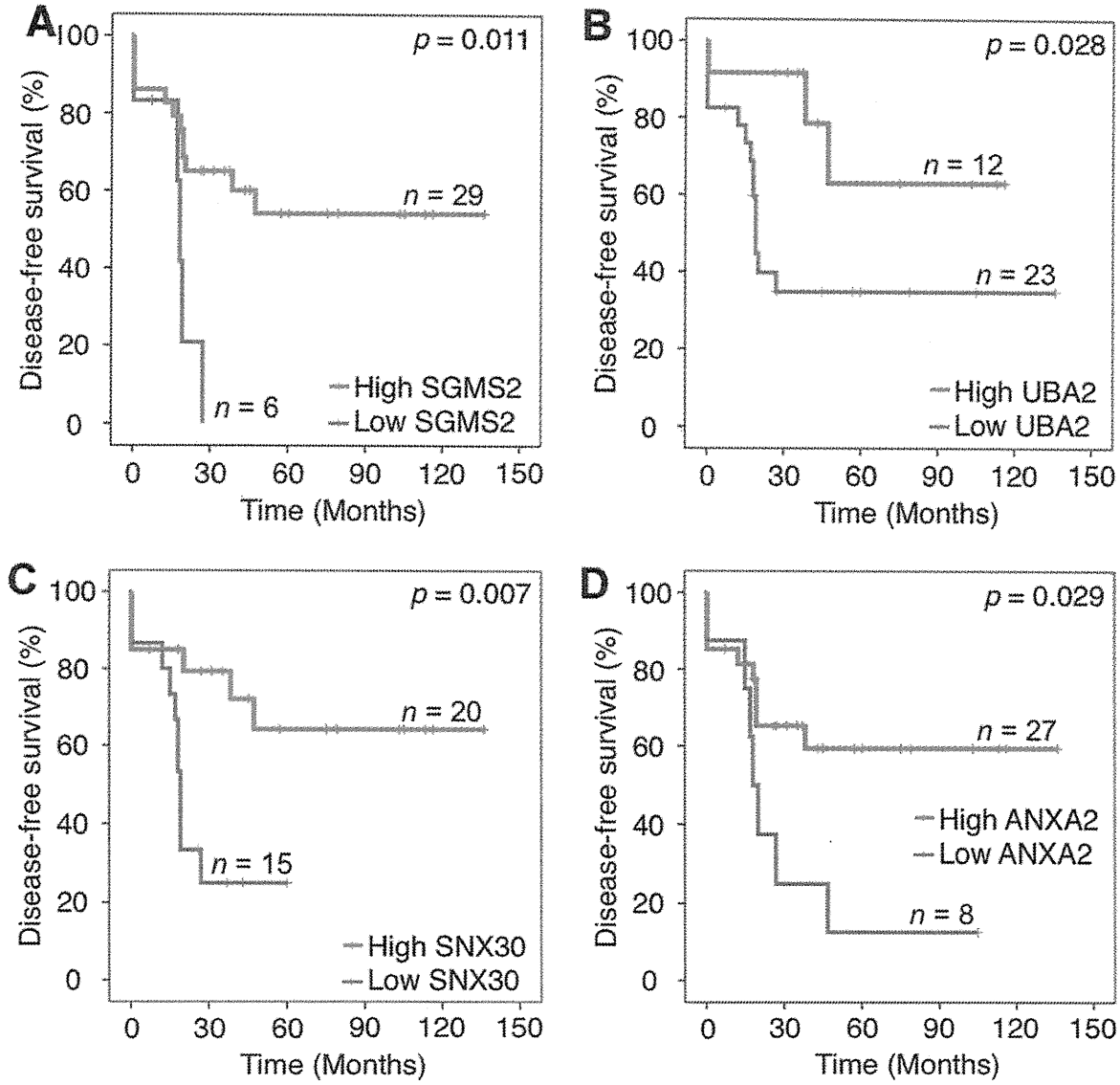

Figure 6. The low expression levels of miR-133a target genes correlate with poor survival of osteosarcoma patients. **(A–D):** Kaplan-Meier survival curves of disease-free survival according to the expression levels of the miR-133a target genes including *SGMS2* (A), *UBA2* (B), *SNX30* (C), *ANXA2* (D) in 35 patient biopsy samples. The optimal cutoff points were determined by the Youden index under the receiver-operating characteristic curve. The statistical significance of differences were determined by the log-rank test. Abbreviations: ANAX2, annexin A2; SGMS2, sphingomyelin synthase 2; SNX30, sorting nexin family member 30; UTR, untranslated region; UBA2, ubiquitin-like modifier activating enzyme 2.

1 showed only a little efficacy on invasiveness in osteosarcoma cells. The most important miRNA that could regulate the multiple phenotypes of osteosarcoma-initiating cells was miR-133a. Although miR-1 and miR-133a correlate with the proliferation of muscle progenitor cells and promote myogenesis [58], their importance in muscle physiology and disease remains unclear [59]. Indeed, miR-133a may be dispensable for the normal development and function of skeletal muscle because skeletal muscle development and function appears unaffected in miR-133a transgenic mice [59]. In this study, silencing of miR-133a had no toxic effect on muscle, including heart and skeletal muscle *in vivo* (Supporting Information Fig. S7E–S7G). Because the upregulation of miR-133a in osteosarcoma cells did not regulate the expression levels of CD133, we determined that it regulated multiple pathways that are not upstream of CD133 expression. Since the inducible factors of CD133 in osteosarcoma have not been cleared, further investigation of the relationship between the tumor microenvironment and CD133 might be warranted. Indeed, the activation of the hypoxia signaling pathway, for example, has been reported to trigger many pathways important for stem cell maintenance [60–62].

Second, we determined the efficacy of LNA technology, an antisense miRNA inhibitor oligonucleotide, as therapeutics against solid cancer. To date, the efficacy of LNAs against human disease has been reported in hepatitis and lymphoma. For example, LNA-antimiR-122 (Miravirsen, Santaris Pharma, San Diego, CA) effectively treats chimpanzees infected with

hepatitis C virus without any observable resistance or physiological side effects [63]. This treatment has advanced to phase II clinical trials, which emphasizes the strengths of LNA-mediated miR-122 silencing, including high efficacy and good tolerability without adverse effects [64]. The other report represents the preclinical trial of LNA-mediated miR-155 silencing against low-grade B-cell lymphoma [65]. Therefore, our preclinical study contributes to the broad application of LNA treatment including solid tumors. While an effective drug delivery system has been the most challenging remaining consideration for the successful translation of RNAi to the clinic for broad use in patients, the systemic administration of LNA-133a did not need assistance of drug delivery system to decrease the expression of miR-133a. These results are consistent with the results of the trial of LNA against HCV infection, in which the LNA was injected via subcutaneous injection. This preclinical trial will not only provide a novel treatment strategy against osteosarcoma but will also support a wide range of LNA applications against cancers that require the silencing of specific miRNAs.

Third, the multiple targets of miR-133a were identified to have antitumor functions against osteosarcoma with clinical relevance. Using an siRNA-induced gene knockdown system and a 3′ UTR luciferase reporter assay, we identified *SGMS2*, *UBA2*, *SNX30*, and *ANXA2* as novel antitumor molecules of osteosarcoma. Some of these molecules have been reported their association with other cancers but not for osteosarcoma. *SGMS2*, located on 4q25, is an enzyme that catalyzes the conversion of phosphatidylcholine and ceramide to sphingomyelin and diacylglycerol [66]. The specific activation of *SGMS2* explains the ability of this gene to trigger cell cycle arrest, cell differentiation, and autophagy or apoptosis in cancer cells [47]. *UBA2*, located on 19q12, forms a heterodimer that functions as a small ubiquitin-like modifier (SUMO)-activating enzyme for the sumoylation of proteins [67]. Conjugating SUMO-1, one of the four SUMO isoforms, to wild-type p53 increases the transactivation ability of p53 [45]. *SNX30*, located on 9q32, may mediate membrane association either through the lipid-binding PX domain (a phospholipid-binding motif) or protein-protein interactions. Although *SNX30* has not been well studied in cancer, loss of *SNX1*, one of the *SNX* families, plays a significant role in the development and aggressiveness of human colon cancer, at least partially through increased signaling from the endosomes [46]. In this study, we found correlations between the expression of *SGMS2*, *UBA2*, and *SNX30* and osteosarcoma cell invasion, as well as a close correlation with the prognosis of osteosarcoma patients. *ANXA2*, located on 15q22, belongs to a large family of diverse proteins that are characterized by conserved annexin repeat domains and the ability to bind negatively charged phospholipids in a calcium-dependent manner [68]. The expression levels of *ANXA2* are decreased in a subset of human OS metastases and metastatic lines [69], but the actual role of *ANXA2* in suppressing OS metastasis has remained unclear [37], which was identified as a regulator of osteosarcoma cell invasion. In this study, we were unable to identify the target genes of miR-133a that were involved in cellular proliferation, which is a general characteristic of TICs. This result may provide one explanation for why the difference in the proliferation rate of the $CD133^{high}$ and $CD133^{low}$ cell populations was relatively small. Another reason for this difference may have been heterogeneiety even within the $CD133^{high}$ cell population. Further investigation of additional markers might shed further light on the mechanisms underlying these phenotypes.

The most interesting and surprising results were the close correlations between the clinical behaviors of osteosarcoma and the expression of the factors associated with malignant tumor-initiating phenotypes, including CD133, miR-133a, and the target genes of miR-133a. These results support the importance of silencing of miR-133a during osteosarcoma treatment. Indeed, the target molecules of miR-133a were found to be significant and novel prognostic factors for osteosarcoma patients. Further analyses of these factors, including *SGMS2*, *UBA2*, and *SNX30*, would allow a better understanding of the molecular mechanisms that regulate osteosarcoma progression.

Overall, our study represents a novel approach for the use of RNAi therapeutics against the lethal phenotype of osteosarcoma. To the best of our knowledge, this study is the first preclinical trial of RNAi therapy overcoming the sarcoma malignancy. We found that miR-133a, which was induced by chemotherapy treatment, is a key regulator of cell invasion of the malignant cell population within osteosarcoma. In a preclinical *in vivo* experiment, systemic administration of LNA-133a with chemotherapy suppressed the osteosarcoma metastasis via the multiple pathways without any significant toxicity. Silencing of miR-133a may therefore represent a novel therapeutic strategy against osteosarcoma, which would lead to an improvement in the prognosis of osteosarcoma patients.

Conclusion

Silencing of miR-133a reduced the malignancy of $CD133^{high}$ osteosarcoma-initiating cell population through restoring the expression of multiple target genes. Systemic administration of LNA-133a with CDDP reduced lung metastasis and prolonged the survival of osteosarcoma-bearing mice. A clinical study revealed that high miR-133a expression levels within the patient biopsy specimens were significantly correlated with poor prognosis, providing the importance of regulating miR-133a levels in osteosarcoma for more efficient therapy in future.

Acknowledgments

We thank T. Yamada for the cDNA library of osteosarcoma clinical samples. We also thank A. Inoue for her technical work. This work was supported in part by a grant-in-aid for the Third-Term Comprehensive 10-Year Strategy for Cancer Control of Japan, the Program for Promotion of Fundamental Studies in Health Sciences of the National Institute of Biomedical Innovation of Japan (NiBio), and a grant-in-aid for Scientific Research on Applying Health Technology from the Ministry of Health, Labor and Welfare of Japan.

Author contributions

T.F.: performed the experimental work, data analysis, and writing of the draft of the manuscript; T.K., K.H., and Y.Y.:

provided the technical skills for the *in vitro* assay; N.K. and R.T.: participated in the conception, design, and coordination of the study; F.T.: provided the technical skills for the *in vivo* LNA delivery; D.K., I.K., A.Y., and E.K.: provided osteosarcoma biopsy samples and their information; H.I.: provided osteosarcoma cell lines from clinical samples resected at the National Cancer Center Hospital of Japan. A.K. and T.O.: initiated the project and provided helpful discussion. The manuscript was finalized by T.O. with the assistance of all authors.

Disclosure of Potential Conflicts of Interest

The authors indicate no potential conflicts of interest.

References

1 Aogi K, Woodman A, Urquidi V et al. Telomerase activity in soft-tissue and bone sarcomas. Clin Cancer Res 2000;6:4776–4781.

2 Fletcher CD. The evolving classification of soft tissue tumours: An update based on the new WHO classification. Histopathology 2006;48:3–12.

3 Naka N, Takenaka S, Araki N et al. Synovial sarcoma is a stem cell malignancy. Stem Cells 2010;28:1119–1131.

4 Reya T, Morrison SJ, Clarke MF et al. Stem cells, cancer, and cancer stem cells. Nature 2001;414:105–111.

5 Clarke MF, Dick JE, Dirks PB et al. Cancer stem cells—Perspectives on current status and future directions: AACR Workshop on cancer stem cells. Cancer Res 2006;66: 9339–9344.

6 Clevers H. The cancer stem cell: Premises, promises and challenges. Nat Med 2011;17:313–319.

7 Visvader JE, Lindeman GJ. Cancer stem cells in solid tumours: Accumulating evidence and unresolved questions. Nat Rev Cancer 2008;8:755–768.

8 Allison DC, Carney SC, Ahlmann ER et al. A meta-analysis of osteosarcoma outcomes in the modern medical era. Sarcoma 2012; 2012:704872.

9 Kawaguchi N, Ahmed AR, Matsumoto S et al. The concept of curative margin in surgery for bone and soft tissue sarcoma. Clin Orthop Relat Res 2004:165–172.

10 Gupta A, Meswania J, Pollock R et al. Non-invasive distal femoral expandable endoprosthesis for limb-salvage surgery in paediatric tumours. J Bone Joint Surg 2006;88: 649–654.

11 Bacci G, Rocca M, Salone M et al. High grade osteosarcoma of the extremities with lung metastases at presentation: Treatment with neoadjuvant chemotherapy and simultaneous resection of primary and metastatic lesions. J Surg Oncol 2008;98:415–420.

12 Halldorsson A, Brooks S, Montgomery S et al. Lung metastasis 21 years after initial diagnosis of osteosarcoma: A case report. J Med Case Rep 2009;3:9298.

13 Adhikari AS, Agarwal N, Wood BM et al. CD117 and Stro-1 identify osteosarcoma tumor-initiating cells associated with metastasis and drug resistance. Cancer Res 2010; 70:4602–4612.

14 Basu-Roy U, Seo E, Ramanathapuram L et al. Sox2 maintains self renewal of tumor-initiating cells in osteosarcomas. Oncogene 2012;31:2270–2282.

15 Gibbs CP, Kukekov VG, Reith JD et al. Stem-like cells in bone sarcomas: Implications for tumorigenesis. Neoplasia 2005;7:967–976.

16 Levings PP, McGarry SV, Currie TP et al. Expression of an exogenous human Oct-4 promoter identifies tumor-initiating cells in osteosarcoma. Cancer Res 2009;69:5648–5655.

17 Siclari VA, Qin L. Targeting the osteosarcoma cancer stem cell. J Orthop Surg Res 2010;5:78.

18 Tirino V, Desiderio V, d'Aquino R et al. Detection and characterization of CD133+ cancer stem cells in human solid tumours. PloS one 2008;3:e3469.

19 Tirino V, Desiderio V, Paino F et al. Human primary bone sarcomas contain CD133+ cancer stem cells displaying high tumorigenicity in vivo. FASEB J 2011;25: 2022–2030.

20 Wilson H, Huelsmeyer M, Chun R et al. Isolation and characterisation of cancer stem cells from canine osteosarcoma. Vet J 2008; 175:69–75.

21 Wu C, Wei Q, Utomo V et al. Side population cells isolated from mesenchymal neoplasms have tumor initiating potential. Cancer Res 2007;67:8216–8222.

22 Gregory RI, Shiekhattar R. MicroRNA biogenesis and cancer. Cancer Res 2005;65: 3509–3512.

23 Ambros V. microRNAs: Tiny regulators with great potential. Cell 2001;107:823–826.

24 Calin GA, Croce CM. MicroRNA signatures in human cancers. Nat Rev Cancer 2006;6:857–866.

25 Esquela-Kerscher A, Slack FJ. Oncomirs—MicroRNAs with a role in cancer. Nat Rev Cancer 2006;6:259–269.

26 Ma S, Tang KH, Chan YP et al. miR-130b Promotes CD133(+) liver tumor-initiating cell growth and self-renewal via tumor protein 53-induced nuclear protein 1. Cell Stem Cell 2010;7:694–707.

27 Calin GA, Ferracin M, Cimmino A et al. A MicroRNA signature associated with prognosis and progression in chronic lymphocytic leukemia. New Engl J Med 2005;353:1793–1801.

28 Jiang J, Gusev Y, Aderca I et al. Association of microRNA expression in hepatocellular carcinomas with hepatitis infection, cirrhosis, and patient survival. Clin Cancer Res 2008;14:419–427.

29 Kawai A, Ozaki T, Ikeda S et al. Two distinct cell lines derived from a human osteosarcoma. J Cancer Res Clin Oncol 1989;115: 531–536.

30 Osaki M, Takeshita F, Sugimoto Y et al. MicroRNA-143 regulates human osteosarcoma metastasis by regulating matrix metalloprotease-13 expression. Mol Ther 2011;19:1123–1130

31 Youden W. Index for rating diagnostic tests. Cancer 1950;3:32–35.

32 Gires O. Lessons from common markers of tumor-initiating cells in solid cancers. Cell Mol Life Sci 2011;68:4009–4022.

33 Cao Y, Zhou Z, de Crombrugghe B et al. Osterix, a transcription factor for osteoblast differentiation, mediates antitumor activity in murine osteosarcoma. Cancer Res 2005;65: 1124–1128.

34 de Crombrugghe B, Lefebvre V, Behringer RR et al. Transcriptional mechanisms of chondrocyte differentiation. Matrix Biol 2000;19:389–394.

35 Ducy P, Zhang R, Geoffroy V et al. Osf2/Cbfa1: A transcriptional activator of osteoblast differentiation. Cell 1997;89:747–754.

36 Nakashima K, Zhou X, Kunkel G et al. The novel zinc finger-containing transcription factor osterix is required for osteoblast differentiation and bone formation. Cell 2002;108: 17–29.

37 Tang N, Song WX, Luo J et al. Osteosarcoma development and stem cell differentiation. Clin Orthop Relat Res 2008;466:2114–2130.

38 Croce CM. Causes and consequences of microRNA dysregulation in cancer. Nat Rev. Genet 2009;10:704–714.

39 Elmen J, Lindow M, Schutz S et al. LNA-mediated microRNA silencing in non-human primates. Nature 2008;452:896–899.

40 Haraguchi T, Nakano H, Tagawa T et al. A potent 2′-O-methylated RNA-based microRNA inhibitor with unique secondary structures. Nucleic Acids Res 2012;40:e58.

41 Obad S, dos Santos CO, Petri A et al. Silencing of microRNA families by seed-targeting tiny LNAs. Nat Genet 2011;43:371–378.

42 Dass CR, Ek ET, Choong PF. Human xenograft osteosarcoma models with spontaneous metastasis in mice: Clinical relevance and applicability for drug testing. J Cancer Res Clin Oncol 2007;133:193–198.

43 Kimura K, Nakano T, Park Y-B et al. Establishment of human osteosarcoma cell lines with high metastatic potential to lungs and their utilities for therapeutic studies on metastatic osteosarcoma. Clin Exp Metastasis 2002;19:477–486.

44 Tsuchida R, Das B, Yeger H et al. Cisplatin treatment increases survival and expansion of a highly tumorigenic side-population fraction by upregulating VEGF/Flt1 autocrine signaling. Oncogene 2008;27:3923–3934.

45 Gostissa M, Hengstermann A, Fogal V et al. Activation of p53 by conjugation to the ubiquitin-like protein SUMO-1. EMBO J 1999; 18:6462–6471.

46 Nguyen LN, Holdren MS, Nguyen AP et al. Sorting nexin 1 down-regulation promotes colon tumorigenesis. Clin Cancer Res 2006;12:6952–6959.